Temperature-vacuum swing adsorption for direct air capture by using low-grade heat

W.K. Shi [a], X.J. Zhang [a], X. Liu [b], S. Wei [c], X. Shi [d], C. Wu [e], L. Jiang [a],*

[a] *Key Laboratory of Clean Energy and Carbon Neutrality of Zhejiang Province, Institute of Refrigeration and Cryogenics, Zhejiang University, Hangzhou, China*
[b] *Institute for Development of Energy for African Sustainability, University of South Africa, Private Bag X6, South Africa*
[c] *The Bartlett School of Sustainable Construction, University College London, 1-19 Torrington Place, London, UK*
[d] *College of Architecture and Urban Planning, Tongji University, Shanghai, China*
[e] *School of Chemistry and Chemical Engineering, Queens University Belfast, Belfast, UK*

ARTICLE INFO

ABSTRACT

Direct air capture (DAC) is a promising carbon mitigation technology and will likely be part of extensive carbon removal portfolio. Adsorptive DAC is an appropriate option for carbon capture to utilize low-grade heat because of its desirable regeneration temperature and adaptability to be integrated with renewables. Building indoor environment with CO_2 concentrations above 1000 ppm provides another suitable scenario for DAC. Herein, DAC using temperature-vacuum swing adsorption (TVSA) is presented and analyzed by integrating various low-grade heat sources in buildings. An amine-functionalized metal organic framework is selected for process simulation, and the performance is compared with those using other sorbents. It indicates that amine-functionalized material has advantages in CO_2 productivity and purity. A techno-economic analysis is carried out to explore the benefit of the proposed DAC in buildings. The results show that regeneration by heat pumps at 373 K is the most competitive solution and has 176.7 $\$\cdot t_{CO_2}^{-1}$ of the levelized cost of DAC (LCOD). Compared with conventional energy supply, solutions with low-grade heat utilization in buildings could achieve lower carbon intensity and increase by 5.2–25.0% in net LCOD. These results will provide practical guidelines for DAC application with lower energy penalties and costs.

1. Introduction

1.1. Background

Intergovernmental Panel on Climate Change (IPCC) reports that CO_2 concentration in the atmosphere has increased from 280 ppm of pre-industrial level to 412 ppm in 2021 (Erans et al., 2022), which is still rising at a speed of 2 ppm per year (Kasotia, 2007). It is demonstrated that rapid decarbonization in energy-related services tends to be insufficient to keep global mean temperature increase well below 2 °C by the end of the 21st century. Carbon dioxide removal (CDR) technologies significantly reduce existing carbon reserves to control atmospheric temperature efficiently.

Direct air capture (DAC) is gathering momentum as an emerging CDR strategy, considered a promising climate change mitigation method. Compared to conventional pre-combustion, oxy-fuel, and post-combustion carbon capture from large point sources such as coal-fired power plant flue gas (Jiang et al., 2019), roughly half of annual CO_2 emission is derived from distributed carbon sources in residences, stores, and buildings, especially in the atmosphere air. Thus, DAC has a unique advantage in that it can be deployed anywhere, capturing CO_2 from distributed sources (Jiang et al., 2023). Compared with bioenergy with carbon capture and storage (BECCS), DAC is expected to have much lower footprints in water and land uses, reducing concerns around food security and biodiversity loss.

Various approaches to technical realization of DAC process have been proposed, among which the vast majority of DAC development is based on sorption processes (Ozkan et al., 2022a). Absorption with alkaline solutions is the first to reach a commercial scale. It is currently the most advanced technology for CO_2 capture from power plants, which tends to consider applying this technology in DAC. However, absorption of diluted CO_2 requires a high air flux and releases considerable reaction heat, which results in water loss of solutions by evaporation (Zeman, 2007). Besides, the absorption method has some noticeable defects, such as unavoidable equipment corrosion, high

Abbreviations

CO_2	Carbon dioxide
DAC	Direct air capture
HVAC	Heating, Ventilation, and Air Conditioning
LCOD	Levelized cost of DAC
LDF	Linear driving force
MOF	Metal organic framework
N_2	Nitrogen
O_2	Oxygen
TVSA	Temperature-vacuum swing adsorption

Symbols

C	Concentration (%)
$C_{p,g}$	Specific heat of gas phase $(kJ \cdot kg^{-1} \cdot K^{-1})$
$C_{p,w}$	Specific heat of wall $(kJ \cdot kg^{-1} \cdot K^{-1})$
D_{ax}	Axial mass diffusivity $(m^2 \cdot s^{-1})$
D_m	Molecular diffusivity $(m^2 \cdot s^{-1})$
D_{ij}	Binary molecular diffusivity of specie i and j $(m^2 \cdot s^{-1})$
ΔH_i	Heat of adsorption of gas specie $(kJ \cdot mol^{-1})$
$k_{ad,i}$	Reaction kinetics of intracrystalline diffusion in micropore of specie (s^{-1})
k_{eff}	Effective thermal conductivity $(W \cdot m^{-1} \cdot K^{-1})$
k_g	Thermal conductivity of gas phase $(W \cdot m^{-1} \cdot K^{-1})$
k_s	Thermal conductivity of sorbents $(W \cdot m^{-1} \cdot K^{-1})$
p	Pressure (Pa)
P_{ev}	Evacuation pressure of vacuum pump (Pa)
q	Adsorption loading $(mol \cdot kg^{-1})$
$q_{CO_2,start}$	Adsorption loading at the start of the TVSA cycle $(mmol \cdot g^{-1})$

R	Universal gas constant $(J \cdot mol^{-1} \cdot K^{-1})$
R_g	Specific gas constant $(J \cdot kg^{1} \cdot K^{-1})$
R_p	Particle radius (m)
T	Temperature (K)
y	Mass fraction

Greek letters

ε	Porosity/void fraction
ρ	Density $(kg \cdot m^{-3})$
μ	Viscosity $(kg \cdot m^{-1} \cdot s^{-1})$

Subscripts

ad	Adsorption
avg	Average
ax	Axial
b	Bed
cool	Cooling
des	Desorption
eq	Equilibrium
ev	Evacuation
g	Gas
i	Index of gas species
L	Linear driving force
op	Operation
out	Outlet
p	Particle
ph	Preheating
s	Sorbent
step	Step point
w	Wall

regeneration temperature (~300 °C) and energy (~200 kJ mol^{-1}) (Fasihi et al., 2019), easy degradation, and low volume absorption ratio. All these challenges shift attention from absorption to adsorption processes, which could partially offset the defects of absorption.

Adsorptive DAC is acknowledged as a good candidate for efficient carbon capture. Several critical issues in DAC need to be addressed, including low-pressure air contactor, CO_2 sorption thermodynamics, rapid kinetics, low regeneration energy and low DAC cost (Board et al., 2019). To date, research and projects are underway to tackle these challenges, mainly with a focus on material development and process modeling.

1.2. Materials and processes for DAC

Currently, adsorbents for DAC have a narrow range when considering high selectivity and fast kinetics. Common physical sorbents, zeolite or activated carbon, are of low equilibrium (<1.0 mmol g^{-1}) under diluted concentration with high nitrogen adsorbed (Mukherjee et al., 2019). Porous materials can adsorb CO_2 by physically impregnating, chemically grafting, or in situ polymerizing amines. This method may impede CO_2 diffusivity. By adjusting the length of the ligands or decorating open sites, metal organic frameworks (MOFs) can be tailored to adsorb CO_2 molecules effectively (Ozkan et al., 2022a). Common MOFs used for post-combustion, such as Mg-MOF-74 (Ben-Mansour and Qasem, 2018), HKUST-1 (Al-Janabi et al., 2015), or MOF-177 (Qasem et al., 2018), have low adsorption equilibrium and are unsuitable for DAC application. Leonzio et al. (2022) uncovered the effect of equilibrium loading on energy penalty, capacity, and investment of DAC, which indicates that MOFs are impracticable and amine-functionalized sorbents are preferred. McDonald et al. (2015) reported an alkylamine-functionalized MOF, mmen-Mg$_2$(dobpdc), with an "S-shape" isotherm and an extraordinary CO_2 adsorption amount of 3 mmol g^{-1},

by appending with N,N-dimethyl ethylene diamine and ethylene diamine. A wide range of studies based on material characterization (Darunte et al., 2017; McDonald et al., 2012) and simulation (Darunte et al., 2018; Hefti et al., 2016) concluded that mmen-Mg$_2$(dobpdc) is an attractive sorbent for DAC. For process modeling, cyclic operations, such as pressure swing adsorption (PSA), temperature swing adsorption (TSA), and temperature-vacuum swing adsorption (TVSA), provide opportunities for the actual production of synthesized sorbents. Elfving et al. (2017) simulated working capacity in PSA, TSA, and TVSA under DAC conditions. PSA is unfeasible due to poor capacity lower than 0.5 mmol g^{-1}. TSA is suggested for concentrated CO_2 production, while TVSA is required for high-purity CO_2. Through TVSA, CO_2 molecules and sorbents are decoupled easily with a combination of vacuum and heat, increasing productivity of CO_2. Zhu et al. (2021) designed a steam-assisted temperature vacuum-swing adsorption process for DAC. After optimization, the processing period is shortened by steam purge and produces 4.45 mol kg^{-1} per day of CO_2 with 0.295 MJ mol^{-1} of energy penalty. Wurzbacher et al. (2016) established a transit heat and mass transfer model to simulate TVSA steps of DAC. For typical process conditions, more than 90% of the captured CO_2 can be recovered at >99% purity. Schellevis et al. (2021) studied the TVSA performance of a kg-scale DAC system. Sensitivity analysis shows optimization towards energy penalty needs high sorbent working capacity, and thermal energy fraction covers >50% of energy penalty in the reference case. Hence, the TVSA process is a practical option to achieve high productivity and efficiency on the scale-up application in DAC.

Due to the ultra-diluted CO_2 concentration, DAC also requires a higher energy penalty than that captures CO_2 through flue gases (Lackner, 2013). Thus, efficient and cost-effective solutions to energy supply for DAC are necessary. Li et al. (2015) proposed a DAC system powered by wind energy. However, electricity is supposed to be reduced as a heating source for its high energy grade. With the development of

thermal science, various engineering cases of heat recovery and renewable energy provide practical assistance for better energy configuration. Fahr et al. (2022) assessed the performance of solar, geothermal, woody biomass, wind, and nuclear energy sources to supply power and heat for DAC, and a removal potential of 160~971 $Gt_{CO_2} \cdot year^{-1}$ can be achieved for energy physically available from solar energy. Fasihi et al. (2019) conducted a literature review and techno-economic analysis of available DAC technologies. A case for solid sorbent-based DAC integrated with hybrid PV-Wind-battery systems indicates that cost will reduce from 105 to 60 €·$t_{CO_2}^{-1}$ with waste heat utilization in 2030, and it is suggested that using heat pumps is an appropriate option to recovery waste heat. Owing to the intermittent and volatile of renewable energy, Breyer and Fasihi et al. (Breyer et al., 2020) further presented a DAC model that the heat provided by low-carbon electricity powered heat pump can be balanced or stored in thermal energy storage (TES). TES units buffer heat supply and reduce heat pump capacity, and only account for 7.2% of the annualized cost for the whole system. Consequently, integration with low grade heat is viable to meet energy demand and cut down the cost of DAC.

1.3. DAC applications in built environments

Building environment is a prominent distributed carbon source for DAC. CO_2 concentration in the building environment is stipulated below 1000 ppm in ASHRAE Standard 62 (Persily, 2015). Excessive CO_2 reduces the comfort of living spaces and even endangers human health. DAC can achieve higher productivity and energy efficiency under higher CO_2 concentrations (Zhao et al., 2019). Thus, deploying carbon capture devices in buildings can be a win-win solution to air purification and decarbonization.

The viability of ventilation strategy with carbon capture devices in buildings has been experimentally demonstrated by Kim and co-workers (Kim et al., 2015, 2020). Soletair has started commercial DAC service in buildings and the cost is 1~2 $\cdot day^{-1}$ per employee (Soletair, 2022). For standard ventilation with 3.3 $m^3 s^{-1}$, the DAC unit proposed by Soletair is designed to produce 50 kg_{CO_2} per day in TVSA processes. The method of energy supply is not revealed, but related research indicates that electricity is generated by renewables, while heat is primarily provided by a boiler (E. Bajamundi et al., 2019). The configuration of energy supply can be optimized. Some studies initially introduce low-grade heat or renewables into building DAC. Shen and Yang et al. (Shen and Yang, 2022) propose a solar driven heating solution for indoor CO_2 capture. It also indicates that 40.655 kg CO_2 can be captured in a day for a 40 m^2 room with 39 occupants. In their subsequent research (Shen and Yang, 2023), it also demonstrate that DAC deployment in buildings can reduce energy consumption of ventilation, and a global analysis is conducted to investigate the role that solar can play in carbon capture in buildings. Thus, DAC can create an eco-friendly environment in buildings and offer incentives for climate mitigation. However, the reported work shows a limited options for low-grade heat utilization, indicating an urgent need for the expansion of heat supply methods.

1.4. Current gap and research objectives

From the literature review, research gaps in adsorptive DAC could be summarized as follows:

1. Current adsorptive DAC has a very high energy penalty during regeneration, leaving a large space to utilize renewables or other low-grade heat sources.
2. DAC has been proposed to be applied in buildings, but the technology is not well integrated with potential heat sources in buildings due to limited sorbents and working processes.

To fill the research gaps, it is necessary to target the wise use of low-grade heat to optimize DAC, which could further reduce life-cycle carbon footprint. This work presents the performance of TVSA process for DAC and explores the potential of its cost-effectiveness by integrating various heat sources in buildings, which forms a suggestive method for the upscaling of the integrated system. The research contents of this work are listed as follows: 1. amine-appended MOF, mmen-Mg_2(dobpdc), is employed to evaluate the performance of the TVSA process for DAC. 2. Condensation heat in Heating, Ventilation and Air Conditioning (HVAC) systems and other heat sources, e.g., solar thermal and auxiliary heating by heat pump, are used for DAC in buildings. 3. The levelized cost of DAC (LCOD) for DAC integrated with each heating solution is calculated from a techno-economic perspective.

2. Concept description

In Section 1.2, the research has highlighted the advantages and challenges of deploying DAC in buildings. Analysis of sorbents and process modeling is not yet illustrated. This section proposes the concept of DAC integrated with renewables or low-grade heat in buildings to reduce cost and meet process energy requirements.

Our previous work explored the performance of sorbents with a system recovering condensation heat of HVAC system, indicating the potential for DAC integrated with low-grade heat in buildings (Ji et al., 2023). To extend this, Fig. 1 illustrates the concept of low-grade heat utilization for DAC in buildings. Exhausted air with high CO_2 concentration is collected from HVAC system and drained to the proposed DAC system. A 4-step TVSA process is also illustrated in Fig. 1 for cyclic CO_2 production, which can be divided into adsorption, preheating, evacuation, and cooling. Inlet blowers pressurize purge air to overcome the resistance along the contactor. When sorbents reach equilibrium, the preheating operation starts with hot water by heat transfer through the contactor's periphery until the target regeneration temperature is reached. Water acts as a working fluid for sorbent regeneration. Vacuum pump then switches on, evacuating CO_2 completely. A cooling step is continued to the initial state.

For the proposed concept, the regeneration process of TVSA can be driven by low-grade heat or renewables. According to different regeneration temperatures, viable solutions are presented as follows:

1. Case 1 (323 K): extract condensation heat from HVAC systems in the building. The refrigerant of the HVAC system releases heat in the vapor compression cycle with a working temperature of around 323 K. It alleviates thermal energy burden when sorbents are regenerated effectively.
2. Case 2 (348 K–SIH): obtain heat from solar by individual heating plants. It is feasible to use solar energy by deploying individual heating systems. Buildings with a large surface area can meet the system's land requirements. The following research sets the heating temperature at 348 K.
3. Case 3 (348 K-SDH): use renewable heat provided by solar district heating. If the proposed DAC plants are widely adopted in the city, solar district heating is another option for regenerating sorbents in addition to deploying solar thermal units in a single building. The centralization of heating may reduce the costs on thermal energy to some extent.
4. Case 4 (373 K): utilize waste heat from condenser water of HVAC by heat pumps. It is widely recognized that heat pump is a potential technology for energy grade promotion. The temperature of the condenser water in the HVAC system typically ranges between 30 °C and 40 °C. Heat pumps on the market can raise heating temperatures to 373 K at a low cost of electricity. Heat pumps above 373 K are ready for commercial use (IEA, 2022), and several applications have been achieved in food drying and chemical industry (Jiang et al., 2022).

The method of heating working fluid by natural gas is also applied for further analysis to compare with four solutions. If these options could
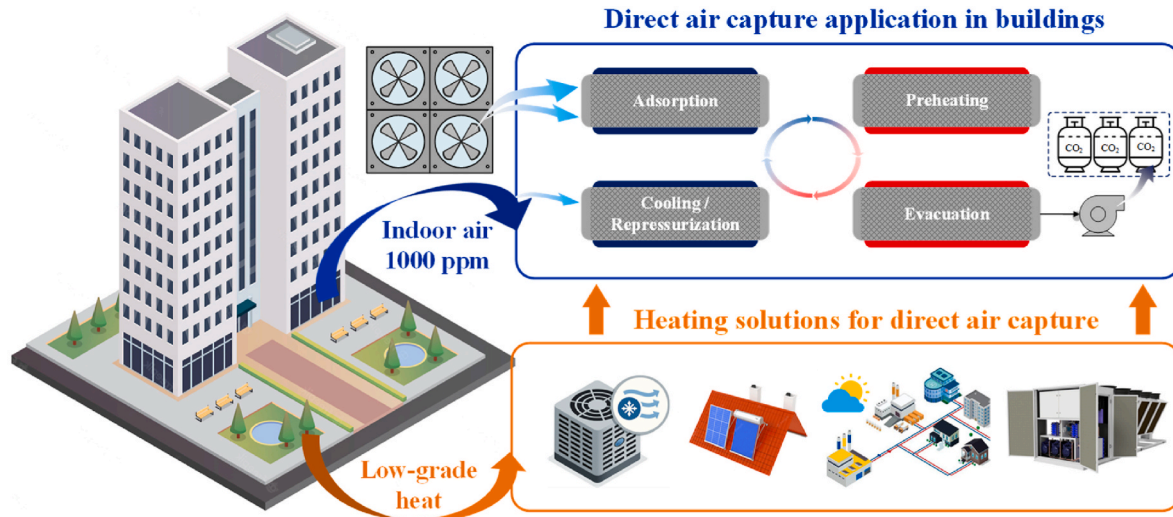
Fig. 1. Concept of low-grade heat utilization for DAC in buildings.

be implemented for the deployment of DAC, energy penalty and cost for CO_2 production would be considerably reduced.

3. Methodology

3.1. Model descriptions

A packed bed model is developed in Section 3 to simulate the temperature profile and mass transfer of DAC. A rectangular geometry in the model is applied for its adaptability to further structural design, such as flatbed (Yu and Brilman, 2020), multi-layer (Rezaei and Webley, 2009), or honeycomb (Wang et al., 2022). The packed bed is assumed to possess a heating jacket through which working fluid flows for regeneration. A thin layer structure is proposed for DAC (Gebald et al., 2017). A single structural unit is stimulated for an adsorption contactor, which can be considered a very short packed bed (Leonzio et al., 2022). Sorbent crystals are assumed to be modeled into particles, and the particles loosely pack in the unit. In Table 1, the parameters of the packed bed are estimated according to similar references. Void fractions of inter-layer and inter-particle space are also considered. CO_2 volume fractions are set at a featured concentration of 0.1% (1000 ppm) for indoor building environments. Cyclic operations of TVSA processes are also conducted in

Table 1
Parameters of the packed bed used in DAC.

Parameters of the packed bed	Value
Bed length, L	50 mm
Bed depth, a	5 mm
Bed width, b	20 mm
Bed porosity, ε_b	0.7 (Darunte, 2018; Hughes et al., 2021)
Particle diameter, d_p	0.5×10^{-3} m (Darunte et al., 2018; Hughes et al., 2021; Pai et al., 2019)
Particle porosity, ε_p	0.35
Wall thickness, d_w	0.001 m
Wall specific heat, $C_{p,w}$	0.5 kJ kg^{-1}·K^{-1}
Wall density, ρ_w	7700 kg m^{-3}
CO_2 volume concentration, C_{CO2}	0.1%
N_2 volume concentration, C_{N2}	78%
O_2 volume concentration, C_{O2}	21.9%
Operating pressure, p_{op}	101325 Pa
Gauge pressure at outlet, p_{out}	0 Pa

the simulation, as shown in Fig. 2.

The model is simulated in ANSYS FLUENT. User Define Functions are used to characterize adsorption/desorption behaviors. The simulated domain is quasi-two-dimensional, and the following assumptions are adopted to simplify the simulation in the packed bed.

(1) Airflow is assumed to be an ideal gas composed of CO_2, N_2, and O_2. Oxygen is considered inert gas for its near-zero capacity in physical sorbents (Wilson and Tezel, 2020).
(2) The sorbent is in a sphere with homogenous, continuous, and temperature/pressure-independent properties.
(3) Gas and solid phase are in local thermal equilibrium with good heat transfer.
(4) Film mass transfer limitation is negligible between the sorbent's surface and bulk concentration.
(5) Working fluid temperature is constant, and heat loss of packed bed is negligible.

3.2. Mathematical model

A packed bed model is established mathematically based on mass transfer, heat transfer, and momentum dissipation in the porous media. Conservation equations are required for the model development. Eq. (1) and Eq. (2) present the overall mass conservation equations.

$$\frac{\partial \varepsilon_b \rho_g}{\partial t} + \nabla(\varepsilon_b \rho_g \overrightarrow{v}) = S_g \tag{1}$$

$$S_g = \sum_i S_{g,i}; \ i \in [CO_2, N_2, O_2] \tag{2}$$

where ρ_g (kg·m^{-3}) is the density of airflow, $\overrightarrow{v}$ (m·s^{-1}) is the velocity vector of airflow, S_g stands for the source term of total mass transfer caused by adsorption/desorption, and $S_{g,i}$ is the source term of mass transfer of each species. Mass conservation of each species can be calculated as Eq. (3).

$$\frac{\partial \varepsilon_b \rho_g y_i}{\partial t} + \nabla(\varepsilon_b \rho_g \overrightarrow{v} y_i) = \nabla(\varepsilon_b D_{ax,i} \nabla(\rho_g y_i)) + S_{g,i} \tag{3}$$

where y_i is mass fraction of each specie, $D_{ax,i}$ (m^2·s^{-1}) is axial mass diffusivity. Gas phase is assumed as plug flow and radial mass diffusivity is ignored. Establishment of $S_{g,i}$ is presented in Eq. (4).

$$S_{g,i} = -(1 - \varepsilon_b)\rho_p M_i \frac{\partial q_i}{\partial t}; \ i \in [CO_2, N_2, O_2] \tag{4}$$

Fig. 2. Schematic diagram of adsorption packed bed and cyclic operations on adsorption isotherm of mmen-Mg$_2$(dobpdc).

where M_i (kg·mol^{-1}) is the mole mass of each specie and $\partial q_i / \partial t$ (mol·kg^{-1}·s^{-1}) is an expression related to adsorption kinetic, which will be further elucidated in Section 3.3. Axial mass diffusivity $D_{ax,i}$ (m^2·s^{-1}) is evaluated by the following empirical correlation (Ruthven, 1984) as Eq. (5).

$$D_{ax,i} = (0.45 + 0.55\varepsilon_b) \cdot D_{m,i} + 0.35R_p v_g \tag{5}$$

where R_p (m) is the radius of particles, and v_g (m·s^{-1}) is gas phase velocity. Molecular diffusivity $D_{m,i}$ (m^2·s^{-1}) of each specie is described in Eq. (6) and Eq. (7) (Fuller et al., 1966; Ruthven, 1984).

$$D_{ij} = 0.0101 T^{1.75} \sqrt{\frac{1}{M_i} + \frac{1}{M_j}} \Bigg/ \left(p \left[(v_i)^{1/3} + (v_j)^{1/3} \right]^2 \right); \ i,j \in [CO_2, N_2, O_2] \tag{6}$$

$$D_{m,i} \Big/ (1 - y_i) = \left(\sum_{j \neq i} y_j / D_{i,j} \right)^{-1} \tag{7}$$

where D_{ij} (m^2·s^{-1}) is the binary molecular diffusivity of specie i and j, v_i (cm^3·mol^{-1}) is the diffusion volume of each specie, and p (Pa) is the absolute pressure of the gas phase.

Momentum conservation of gas phase is shown in Eq. (8) and Eq. (9).

$$\frac{\partial(\rho_g \vec{v})}{\partial t} + \nabla(\rho_g \vec{v}) = -\nabla p + \nabla(\bar{\bar{\tau}}) + \rho_g \vec{g} + \vec{F} \tag{8}$$

$$\vec{F} = 150 \frac{\mu_g (1 - \varepsilon_b)^2}{\varepsilon_b^3 d_p^2} \vec{v} + 1.75 \frac{(1 - \varepsilon_b)}{\varepsilon_b^3 d_p} \rho_g |\vec{v}| \vec{v} \tag{9}$$

where p (Pa) is local pressure of gas, $\bar{\bar{\tau}}$ (N·m^{-2}) is gas phase shear stress, $\vec{g}$ (m^2·s^{-1}) is vector of gravitational acceleration. $\vec{F}$ (Pa·m^{-1}) is expressed as a momentum source term contributed by viscous loss and inertial loss and can be calculated by Ergun equation (Ben-Mansour et al., 2016) as shown in Eq. (9) where μ_g (kg·m^{-1}·s^{-1}) is gas viscosity, d_p (m) is the diameter of the particle.

The equilibrium and non-equilibrium thermal models can be used for energy conservation. Thermal equilibrium considers that gas and solid phase are kept at the same temperatures. Li et al. (2018) compare two methods with breakthrough curves. The results indicate that the equilibrium model can save computational costs for simulations at the expense of tolerable accuracy loss. A series of research (Ben-Mansour and Qasem, 2018; Lian et al., 2019; Schellevis et al., 2021) has adopted the equilibrium model and got robust results. The energy conservation equation is given by Eq. (10).

$$\frac{\partial T}{\partial t} \left(\varepsilon_b \rho_g C_{p,g} + (1 - \varepsilon_b)\rho_s C_{p,s} \right) + \nabla \left((\rho_g C_{p,g} + p) \vec{v} \right)$$
$$= \nabla \cdot \left(k_{eff} \nabla T + (\bar{\bar{\tau}} \cdot \vec{v}) - \left(\sum_i h_i J_i \right) \right) + \sum_i S_{ad,i} \tag{10}$$

where $C_{p,g}$ (J·kg^{-1}·K^{-1}) is specific heat of gas phase, $C_{p,w}$ (J·kg^{-1}·K^{-1}) is specific heat of sorbents, ρ_s (kg·m^{-3}) is the density of sorbents. h_i (J·kg^{-1}) and J_i (kg·m^{-2}·s^{-1}) is sensible enthalpy and diffusion flux of each gas specie, respectively. $\sum_i S_{ad,i}$ represents the sum of the source term of energy discharge/charge during adsorption/desorption steps, which are calculated in Eq. (11). Effective thermal conductivity k_{eff} (W·m^{-1}·K^{-1}) is expressed in Eq. (12).

$$\sum_i S_{ad,i} = (1 - \varepsilon_p)\rho_s \sum_i \Delta H_i \frac{\partial q_i}{\partial t} \tag{11}$$

$$k_{eff} = \varepsilon_b k_g + (1 - \varepsilon_b) k_s \tag{12}$$

where ΔH_i (kJ·mol^{-1}) is adsorption heat, k_g and k_s are the thermal conductivity of sorbents and gas phase. The conservation equations are solved using ANSYS FLUENT by finite volume method. Thermal conductivity and viscosity of the gas phase are determined by mass-weight-mixing-law in FLUENT.

3.3. Adsorption equilibrium and kinetic

Adsorption characteristics are required to develop the model. Experimental data about adsorption equilibrium and kinetic of mmen-Mg$_2$(dobpdc) is obtained from previous research (McDonald et al., 2015; Wu et al.,). Table 2 shows the adsorption and thermal properties of mmen-Mg$_2$(dobpdc).

The sorbent exhibits an "S-shape" adsorption isotherm. A small adsorbed amount of CO$_2$ will change the stability of MOF and induce more CO$_2$ adsorbed, which is called cooperative insertion (McDonald et al., 2012). Hefti et al. (2016) proposed a weighted-dual site Langmuir

Table 2
Adsorption and thermal properties of mmen-Mg$_2$(dobpdc).

Parameters of the packed bed	Value
Thermal conductivity, k_s	0.3 W m^{-1}·K^{-1} (Liu et al., 2012)
Heat capacity of crystal, $C_{p,s}$	1.6 kJ kg^{-1}·K^{-1} (McDonald et al., 2015)
Sorbent density, ρ_s	860 kg m^{-3} (Darunte et al., 2018; Hefti et al., 2016)
Sorbent porosity, ε_p	0.35 (Pai et al., 2019)
CO$_2$ adsorption heat, ΔH_{CO2}	71 kJ mol^{-1} (Ozkan et al., 2022a; Zhang et al., 2021)
N$_2$ adsorption heat, ΔH_{N2}	18 kJ mol^{-1} (Ben-Mansour et al., 2017)

isotherm and used a smooth function to fit the step stage of adsorption. Darunte et al. (2018) modified the model and used Sips isotherm to describe CO_2 adsorption before the step stage.

This work mainly focuses on the adsorbed amount of CO_2 and N_2 at a fixed temperature. Thus, the weighted-dual site Langmuir isotherm (see Eq. (13)) is adopted, and a detailed isotherm model is established according to Darunte's work with some modifications, as shown in Eq. (13)~(16).

$$q_{CO_2} = q_{low}(p,T)(1 - w(p,T)) + q_{high}(p,T)w(p,T) \quad (13)$$

$$q_{low} = \frac{q_L(b_L p)^n}{1 + (b_L p)^n} \quad (14)$$

$$q_{high} = \frac{q_H b_H p}{1 + b_H p} + q_U p \quad (15)$$

$$\omega = \left(\exp\left(\frac{\ln(p/p_{step})}{\sigma} \right) \Big/ \left(1 + \exp\left(\frac{\ln(p/p_{step})}{\sigma} \right) \right) \right)^\gamma \quad (16)$$

where q_{CO2} is the adsorption equilibrium loading of sorbent, q_{low} and q_{high} describe the amount absorbed by two adsorption mechanisms caused by CO_2 partial pressure difference, and p is the absolute partial pressure of CO_2. w is a weighted smooth function, q_L, q_H, n, and q_U reflect the homogeneity and affinity of sorbents. p_{step}, σ, and γ are used to calculate w and illustrate the tendency of the step stage. The adsorption equilibrium of N_2 is shaped by Langmuir isotherm, as shown in Eq. (17).

$$q_{N_2} = \frac{a_{N_2} b_{N_2} p}{1 + b_{N_2} p} \quad (17)$$

where q_{N2} is the amount absorbed at equilibrium, a_{N2} is the maximum adsorbed amount, and b_{N2} is a parameter related to the temperature of sorbents. Table 3 presents the value of the involved parameters in the adopted isotherm model, and Table 4 shows the temperature dependence of related parameters.

Fig. 3 presents fitting curves of CO_2 and N_2 adsorption equilibrium with experimental results. Adsorption equilibrium loading of CO_2 at 313 K under 1 mbar comes to 2.89 mmol g^{-1} and is predicted to be 3.31 mmol g^{-1} at 298 K, and tolerable error is 5.08% when compared to experimental data. "S-shape" isotherm and extraordinary adsorption equilibrium make mmen-Mg_2(dobpdc) an ideal sorbent for DAC. Unlike conventional physical sorbents, amine-loaded sorbents usually have low N_2 equilibrium capacity (Baboolal, 2015; Mason et al., 2015). Fig. 3b compares adsorption equilibrium of CO_2 and N_2. It also shows that N_2 equilibrium loading is as low as 0.12 mmol g^{-1} at 1 bar, contributing to high-concentrated CO_2 production.

Linear driving force (LDF) models in Eq. (18) are used to evaluate adsorption kinetics of sorbents.

$$\frac{\partial q_i}{\partial t} = k_{L,i}(q_{eq,i} - q_i); \ i \in [CO_2, N_2] \quad (18)$$

where q_i represents immediate adsorption equilibrium of each specie, $q_{eq,i}$ is equilibrium loading of each specie and $k_{L,i}$ is mass transfer constant of LDF model. Mass transfer resistance can be attributed to macropore diffusion and adsorption reaction in micropores.

Mass transfer constants for CO_2 and N_2 are evaluated by Eq. (19) and Eq. (20) (Farooq and Ruthven, 1990).

$$\frac{1}{k_{L,CO_2}} = \frac{d_p^2}{60\varepsilon_p D_{eff,CO_2}} + \frac{1}{k_{ad,CO_2}}; \ \text{For } CO_2 \quad (19)$$

$$\frac{1}{k_{L,N_2}} = \frac{d_p^2}{60\varepsilon_p D_{eff,N_2}}; \ \text{For } N_2 \quad (20)$$

where $k_{ad,CO2}$ is reaction kinetic of intracrystalline diffusion in micropore. $D_{eff,CO2}$ and $D_{eff,N2}$ are effective intercrystalline diffusivity of CO_2 and N_2, respectively, evaluated in Table S1. For N_2 adsorption, intercrystalline diffusivity is the dominant factor for overall mass transfer (Dantas et al., 2011; Patton et al., 2004). $k_{ad,CO2}$ is a parameter of temperature dependence for 1000 ppm referred to a standard Arrhenius equation given by Eq. (21).

$$k_{ad,CO_2} = A \exp\left(\frac{\Delta E_{ad}}{RT_0} \left(1 - \frac{T_0}{T} \right) \right) \quad (21)$$

where A, ΔE_{ad} and T_0 are parameters fitted from experimental results, listed in Table S1. The estimation results of overall mass transfer constants are presented in Fig. 4 when compared to experimental data. Adsorption kinetic is the same scope as previous amine-loaded sorbents (Brilman et al., 2013; Miao et al., 2021; Zhu et al., 2021). The results show the overall mass transfer constants are 0.0038 s^{-1} and 0.0164 s^{-1} at 298 K and 373 K, respectively. The kinetics of different desorption temperatures are predicted by Eq. (19) and Eq. (21).

3.4. Performance indicator

The involved performance indicators of 4-step TVSA process are average adsorption equilibrium $q_{avg,CO2}$ (mol·$kg_{sorbent}^{-1}$), productivity (kg_{CO2}·$kg_{sorbent}^{-1}$·day^{-1}), and purity of the concentrated CO_2, calculated as Eq. (22)~(24).

Table 3
The adsorption isotherm model of CO_2 and N_2 (Darunte, 2018; Darunte et al., 2018).

Parameters	Value	Parameters	Value	Parameters	Value
T_0	313.15 K	ΔH_{N2}	18000 J mol^{-1}	λ_1	0.036
$p_{step,0}$	51 Pa	ΔH_{step}	74290 J mol^{-1}	λ_2	0
q_L	28.25 mol kg^{-1}	ΔH_L	70740 J mol^{-1}	n_0	0.53
q_H	3.5 mol kg^{-1}	ΔH_n	1351 J mol^{-1}	$b_{L,0}$	2.5×10^{-17} Pa^{-1}
$q_{U,0}$	5.33×10^{-9} mol kg^{-1}	ΔH_H	67720 J mol^{-1}	$b_{N2,0}$	2.58×10^{-8} Pa^{-1}
a_{N2}	0.154 mol kg^{-1}	ΔH_U	18670 J mol^{-1}	$b_{H,0}$	2.4×10^{-13} Pa^{-1}
R	8.314 J mol^{-1}·K^{-1}				

Table 4
Adsorption parameter of temperature dependence.

Equations		
$p_{step} = p_{step,0} \exp\left(\frac{\Delta H_{step}}{RT_0} \left(1 - \frac{T_0}{T} \right) \right)$	$\sigma = \lambda_1 \exp\left(\frac{\lambda_2}{T_0} \left(1 - \frac{1}{T_g} \right) \right)$	$n = n_0 \exp\left(\frac{\Delta H_n}{RT} \right)$
$b_\alpha = b_{\alpha,0} \exp\left(\frac{\Delta H_\alpha}{RT} \right); \ \alpha \in [L,H,N_2]$		$q_U = q_{U,0} \exp\left(\frac{\Delta H_U}{RT} \right)$
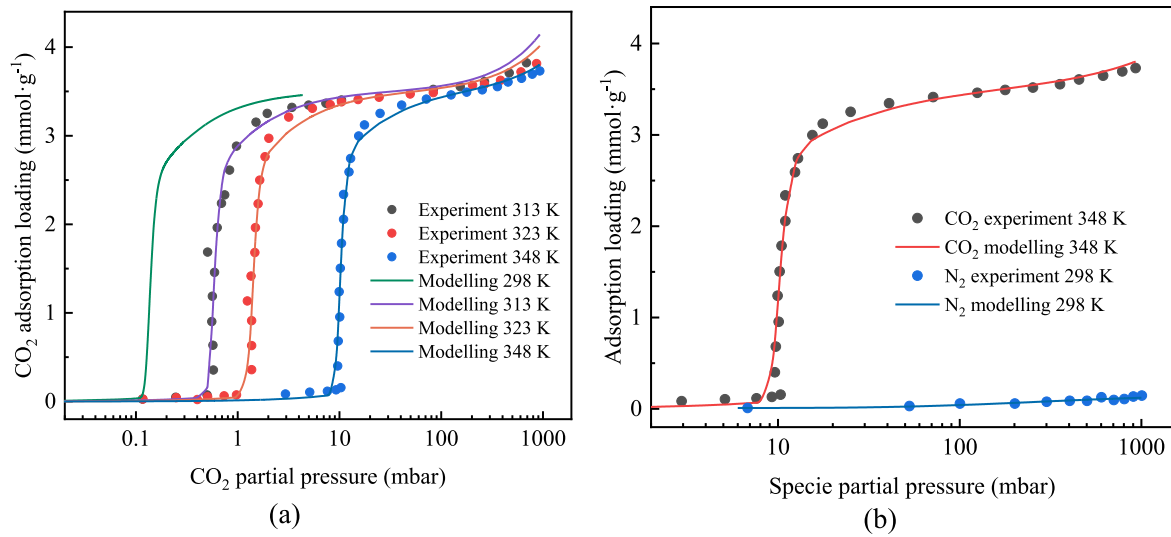
Fig. 3. (a) the fitting isotherms at different temperatures of CO_2 and (b) the isotherm comparison between CO_2 and N_2. Experimental results come from Ref (McDonald et al., 2015). for CO_2 and Ref (Wu, J. et al., 2022). for N_2.
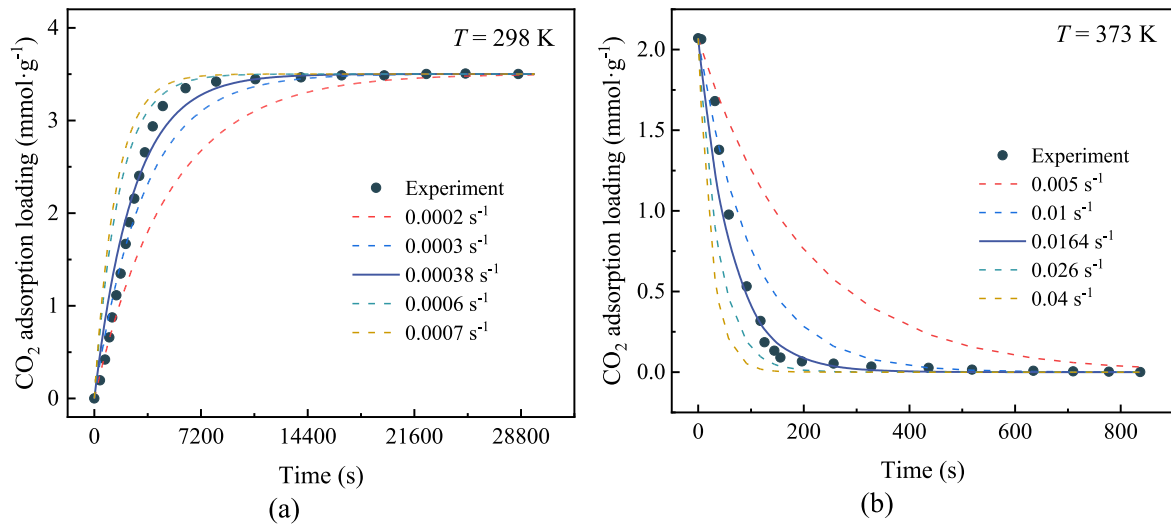
Fig. 4. Fitting kinetics at (a) 298 K of adsorption temperature and (b) 373 K of desorption temperature. Experimental data are obtained from Ref. (Darunte et al., 2018; Wu et al.).

$$q_{avg,CO_2} = \int_0^{V_b} q_{CO_2} \rho_s \varepsilon_b dV_{cell} \Big/ (\rho_s(1-\varepsilon_b)V_b) \qquad (22)$$

$$\text{Productivity} = (t_{day}/t_{cycle}) \cdot \int_0^{t_{des}} m_{purge} CO_2 dt \Big/ (\rho_s(1-\varepsilon_b)V_b) \qquad (23)$$

$$\text{Purity} = \int_0^{t_{des}} m_{purge} CO_2 dt \Big/ \int_0^{t_{des}} m_{purge} dt \qquad (24)$$

where q_{CO2} is adsorption equilibrium loading of each finite volume V_{cell}, and V_b is the assumed packed bed volume. The mass flow rate of purge gas is expressed as m_{purge}. t_{des} and t_{cycle} is the desorption time and total operating time of a TVSA process. t_{day} (s) is the daily working hours for the process. All the parameters can be output from FLUENT.

The total energy penalty of DAC processes can be divided as follows: (1) adsorption heat of CO_2 and N_2; (2) sensible heat of sorbent; (3) sensible heat of gas purged in desorption; (4) energy of auxiliary equipment, including air blower and vacuum pump. The energy penalty of DAC is described in **Supplementary Information Note S1** in detail.

4. Results and discussion

4.1. Bed parameter and working cycle

The operating parameter estimation of the proposed TVSA is presented in this subsection by using mmen-Mg₂(dobpdc). The initial adsorption temperature is set at 298 K. The outer of the packed bed is regarded to be isothermal in the process. Fig. 5a depicts simulated breakthrough curves for various inlet air velocities. Due to insignificant capacity before step pressure, fast velocities and low kinetics of sorbents, all curves undergo shocks of concentration in the first few seconds of adsorption. The trend of concentration ratio from 0 to the first shock is insignificant due to the relatively short period. When the velocity is lower to 0.03 m s⁻¹, the curve reaches a plateau and makes a second shock at 27000 s until sorbents reach adsorption equilibrium. The plateau of curves is more significant under lower velocities. It can be explained by "wave theory", attributed to "S-shape" isotherm (Cousin-Saint-Remi and Denayer, 2017; Darunte et al., 2018). Fig. 5b shows the average CO_2 adsorption loading in the packed bed. The sorbents are not saturated after 21600 s of adsorption at 0.05 m s⁻¹ of inlet air

(a)

(b)

(c)
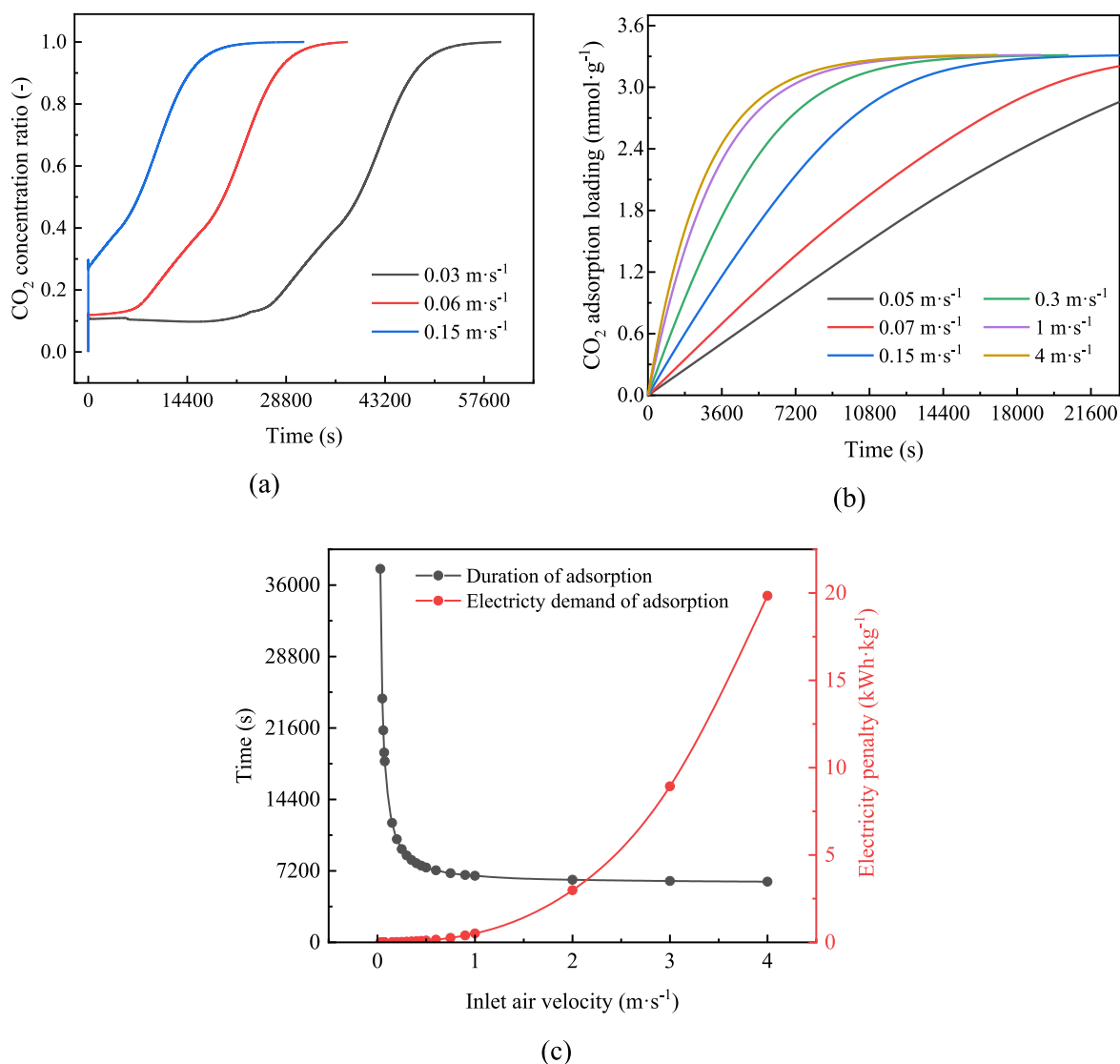
Fig. 5. Simulated results of adsorption step for packed bed at 298 K: (a) breakthrough curve of CO_2; (b) average CO_2 absorbed amount for different inlet air velocities; (c) electricity penalty and period of adsorption step for sorbent to reach 90% of saturated CO_2 equilibrium loading.

velocity. Higher velocities can shorten the period of the adsorption step. For example, at 1 m s^{-1}, the packed bed only takes 6700 s to achieve 90% saturated CO_2 equilibrium loading. However, ultrahigh air velocities exacerbate the electricity consumption of blowers to overcome momentum loss along the packed bed. Fig. 5c illustrates the trade-off between air velocities and electricity penalty. CO_2 adsorption loading at the end of the step is set as 90% of equilibrium loading. Adsorption time reduction caused by increased speed is no longer significant after 1 m s^{-1}, while electricity consumption per mole CO_2 adsorbed will sharply rise.

The wall of the packed bed can be heated or cooled by heat exchangers and is assumed as an isothermal boundary. Desorption is divided into two detailed steps: the packed bed will be pre-heated and then evacuated to lower pressure. The preheating step is conducted to obtain high product purity at a low loss of CO_2 (Wilson, 2022). The results from Fig. 6 show that the bed reaches all target desorption temperatures after 720 s. The bed is sealed, while slight CO_2 release can still occur during heating. The CO_2 loss of sorbent at 373 K is slightly higher than 323 K and 348 K but only accounts for 0.76% of the saturated adsorbed amount and can be neglected.

The evacuation step is needed to pump desorbed CO_2 efficiently. Sorbents are supposed to undergo a sharp drop of CO_2 loading when the
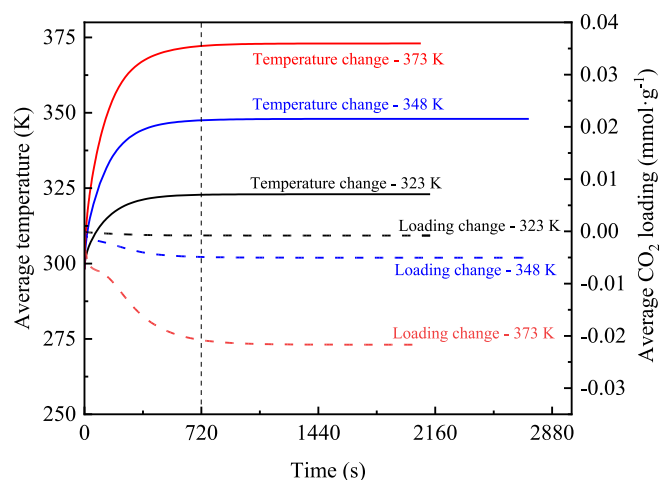
Fig. 6. Simulated results of preheating step for packed bed. Solid lines: average temperature variation for 323 K, 348 K, and 373 K of desorption temperature. Dash lines: average CO_2 adsorption loading variation for different desorption temperatures.
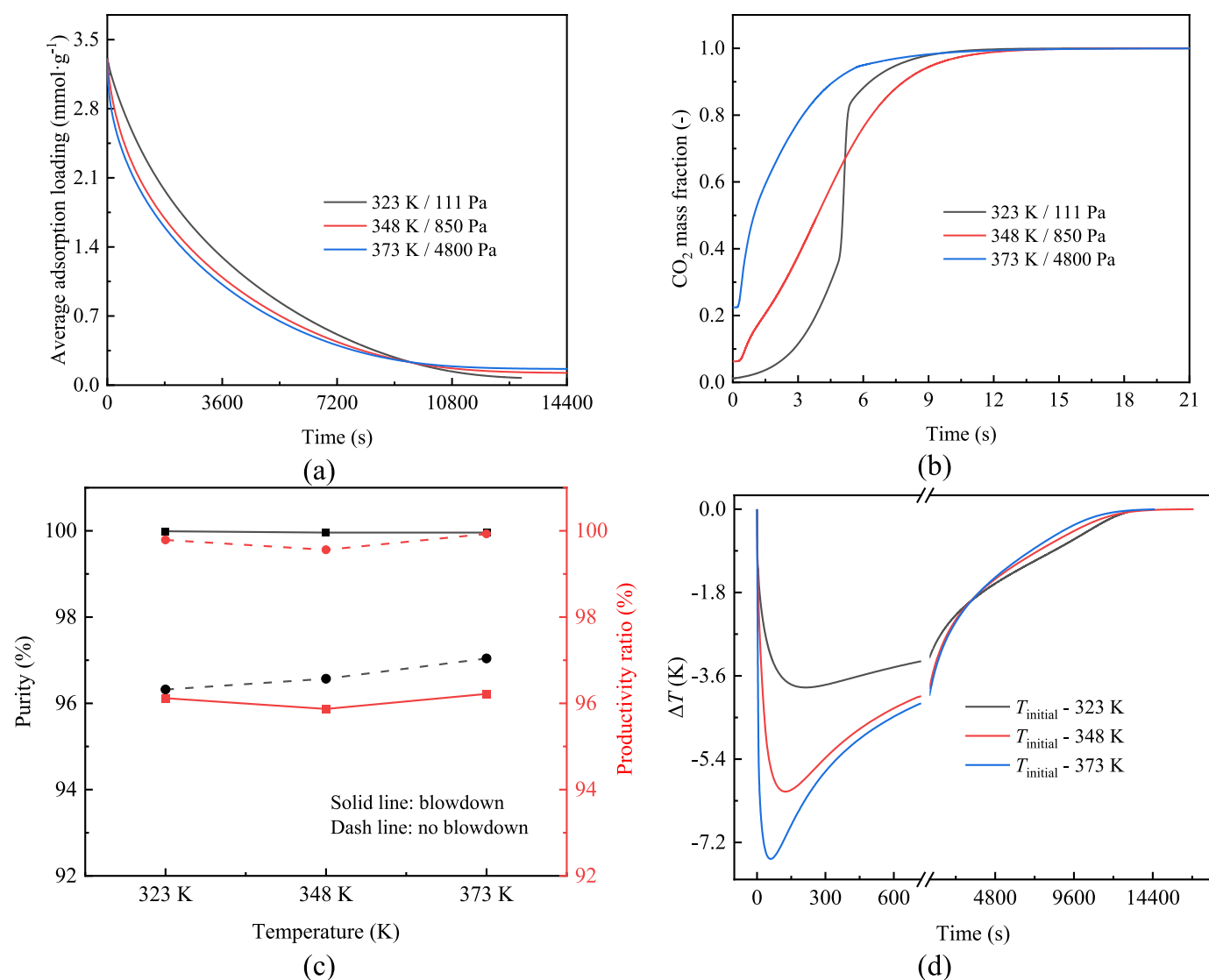
Fig. 7. Performance of evacuation step for packed bed at 323 K, 348 K, and 373 K: (a) variation of average CO_2 adsorption loading; (b) mass fraction CO_2 at the outlet; (c) comparison on purity and productivity between blowdown and no blowdown; (d) variation of the average temperature of sorbent.

pressure in the packed bed is lowered to the step stage at adsorption isotherm. Step pressure is 120 Pa, 880 Pa, and 4950 Pa for 323 K, 348 K, and 373 K, respectively. The related magnitude of vacuum can be achieved by industrial vacuum pumps on the market (Busch, 2022; Copco) under the premise of ensuring good air tightness of packed bed and adsorption contactor. Fig. 7a gives dynamic simulated average CO_2 loading when evacuated at 323 K, 348 K, and 373 K. After 10800 s, over 95% CO_2 can be extracted at a specific pressure. Evacuation at lower pressure has a shorter time cost but also leads to more significant electricity consumption for vacuum pumps. Blowdown is a step operated before CO_2 product harvesting and pre-strips residual N_2 and O_2 of interparticle void in the packed bed.

The CO_2 mass fraction at the outlet is shown in Fig. 7b. It jumps to close to 99.9% within 12 s. The curve at 323 K shows an "S-shape" like the isotherm. The residual CO_2 amount is less desorbed from preheating step at 323 K, and low evacuation pressure induces faster desorption of impurity. It can also be concluded from Fig. S2a and Fig. S2b. Fig. 7c analyzes the influence of blowdown. On a fixed blowdown time at 6 s, the operation enhances purity from ~96% to over 99.9% at 3% product loss. In Fig. 7d, $T_{initial}$ denotes target desorption temperature, and ΔT means average temperature drop from $T_{initial}$. It is also found that the endothermic effect of desorption is more evident as the increased

desorption temperature. It hinders the desorption process of sorbents. These phenomena suggest that low heat of adsorption should also be considered to maintain an effective adsorption reaction when choosing sorbents. Fig. 8 shows the temperature for the cooling step. It indicates 600 s of cooling time is needed to restore adsorption capacity for the second cycle. The analysis describes the cyclic operation of the proposed TVSA process and gives a primary evaluation of process parameters. The estimated duration of each step is summarized in Table 5.

4.2. Comparisons of mmen−Mg₂(dobpdc) and typical sorbents

The primary estimation for process parameters of the proposed TVSA cycle provides a reference for simulations based on other typical sorbents, Zeolite 13X and Mg-MOF-74. Zeolite 13X is a widely used candidate for gas separation and purification. Previous research (Kumar et al., 2015; Ozkan et al., 2022a) shows that Mg-MOF-74 performs better than other coordinately unsaturated MOFs in carbon capture. Adsorption characteristics of Zeolite 13X and Mg-MOF-74 are given in Table S2 and Table S3.

Fig. 9 presents breakthrough curves of three sorbents. Velocities of the feed gas are all fixed at 0.03 m s^{-1}. In Mg-MOF-74 and Zeolite 13X, the overall mass transfer rate is estimated at 0.001 s^{-1} for CO_2 and 0.3
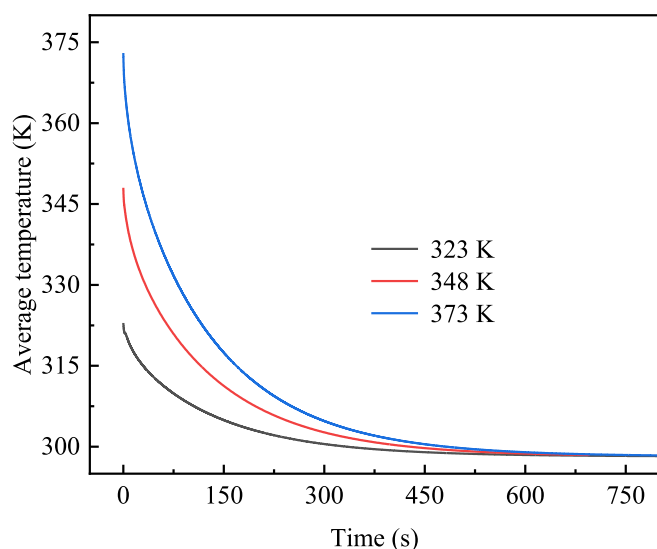
Fig. 8. The simulated average temperature variation of cooling step for packed bed from 323 K, 348 K, and 373 K.

Table 5
The estimated duration for each step of the TVSA process.

Parameters of the packed bed	Duration	Notes
Adsorption	7200 s	0.6 m s^{-1} of air velocity
Preheating	720 s	/
Desorption	10800 s	6 s for blowdown
Cooling	600 s	/
Total	5 h 22 min	/
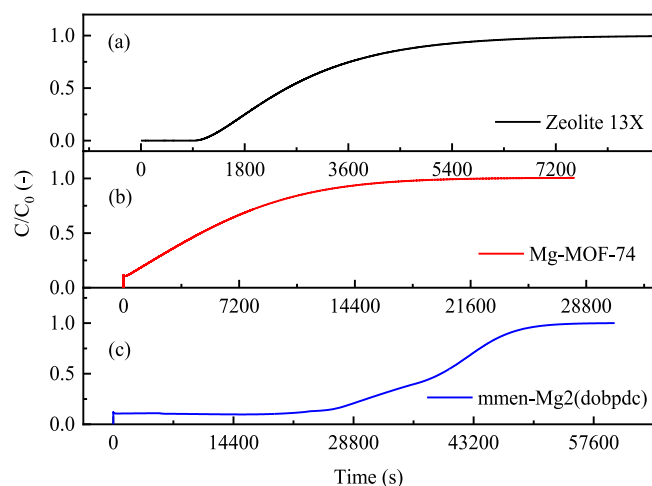
Fig. 9. Simulated breakthrough curves at 298 K for (a) Zeolite 13X, (b) Mg-MOF-74, (c) mmen-Mg$_2$(dobpdc).

s^{-1} for N$_2$. The rates are mainly dominated by macropore diffusivity (Dantas et al., 2011; Ruthven and Xu, 1993). The equilibrium loading of CO$_2$ at 1000 ppm is 0.925 mmol g^{-1} for Zeolite 13X, and 0.345 mmol g^{-1} for Mg-MOF-74. Due to the relatively low CO$_2$ capacity and kinetic of Mg-MOF-74, the outlet of the bed occurs a sudden concentration rise at first seconds after feed gas is supplied. Then the concentration shows continued growth and arrives to be the same as the inlet after the bed is saturated. For Zeolite 13X, the concentration stays constant in the first 900 s. As the gap between instant and equilibrium loading decreases, the adsorption rate slows down and induces the breakthrough of CO$_2$. The

breakthrough tendency of mmen-Mg$_2$(dobpdc) seems like a combination of two other sorbents. The first breakthrough of mmen-Mg$_2$(dobpdc) can be attributed to a sharp drop of the equilibrium loading as concentration decreases along the bed according to its isotherm model. Thus, equilibrium loading is low at the back part of the bed, resulting in CO$_2$ from the front part is not efficiently absorbed. Although the front part is partially saturated as adsorption proceeds, concentrations at the back part increase and the overall equilibrium loading of the bed does not notably decline. Thus, the curve appears to enter a long plateau and bring about a second breakthrough at the end period of adsorption. Breakthrough curves reflect the dynamic adsorption and indicate discrepancies in productivity and purity among these sorbents.

In TVSA process, working capacity is usually lower than equilibrium loading. Simulations for Zeolite 13X and Mg-MOF-74 are conducted to compare the cyclic performance of sorbents. Table S4 summarizes the operation parameters in each simulation. Fig. 10a shows the characteristic of Zeolite 13X and Mg-MOF-74 by plotting CO$_2$ uptake variation as a function of time in multiple cycles. Under evacuation at 4000 Pa and 373 K, the working capacity of Zeolite 13X and Mg-MOF-74 is stable at around 0.123 mmol g^{-1} and 0.033 mmol g^{-1}, respectively. The CO$_2$ loading on mmen-Mg$_2$(dobpdc) can be released almost entirely, achieving a working capacity at 2.659 mmol g^{-1} for a single cycle. The characteristic of the proposed TVSA process makes working capacities for Zeolite 13X and Mg-MOF-74 insignificant. One possible way to overcome this shortcoming is to increase desorption temperature or reduce evacuation pressure, but higher thermal energy penalty and grade deter the process from deploying in buildings.

However, the case of mmen-Mg$_2$(dobpdc) also has a higher time cost. It may adversely affect daily productivity. To further illustrate the priority of mmen-Mg$_2$(dobpdc), Fig. 10b analyzes CO$_2$ purity and daily productivity of all three sorbents. The results show that mmen-Mg$_2$(dobpdc) has the highest daily productivity. The purity of product gas is highly related to the change of N$_2$ loading from adsorption to desorption temperatures. Physisorbents, including Zeolite 13X and Mg-MOF-74, usually face the problem of poor selectivity for CO$_2$ and N$_2$. The purity is 34.96% and 3.81% for Zeolite 13X and Mg-MOF-74, respectively, and the performance of mmen-Mg$_2$(bodpdc) is 97.45%.

The comparison provides a reference for choosing sorbents for DAC. Zeolite 13X has a mature synthesis process and can be easily available in the market. However, low productivity demands larger amounts of sorbents and higher land occupation, moderate CO$_2$ product purity, and low purchasing price make it a good candidate for an application like microalgae cultivation or carbonate mineralization (Hong, 2022). The results suggest that Mg-MOF-74 is unsuitable for DAC considering purity and productivity. Recent studies have designed and synthesized a series of MOFs with hybrid ultra-microporous materials (HUMs) (Kumar et al., 2017). It achieves better cyclic performance by enhancing adsorption capacity and selectivity. Although mmen-Mg$_2$(dobpdc) shows limitations in mass transfer, its high working capacity still makes it a good choice for DAC. The highly concentrated product also indicates a broader range of carbon utilization.

4.3. Energy analysis

Due to the ultra-diluted CO$_2$ concentration in the atmosphere, DAC is an energy-intensive process from the point of thermodynamics compared to conventional gas separation. TVSA cycle has huge thermal energy demand to regenerate sorbents and consumes considerable electricity during evacuation. The calculation method for each equipment is provided in **Supplementary Information Note S1.** The calculation does not consider the accessories like mass flow controllers used in a real application scenario. The energy analysis is conducted at three featured desorption temperatures, 323 K, 348 K, and 373 K, mentioned in Section 2. The case of 373 K uses heat pumps for regeneration, while others directly utilize heat from renewables. Parameters in the calculations are listed in Table S5. CO$_2$ loadings starting desorption are fixed
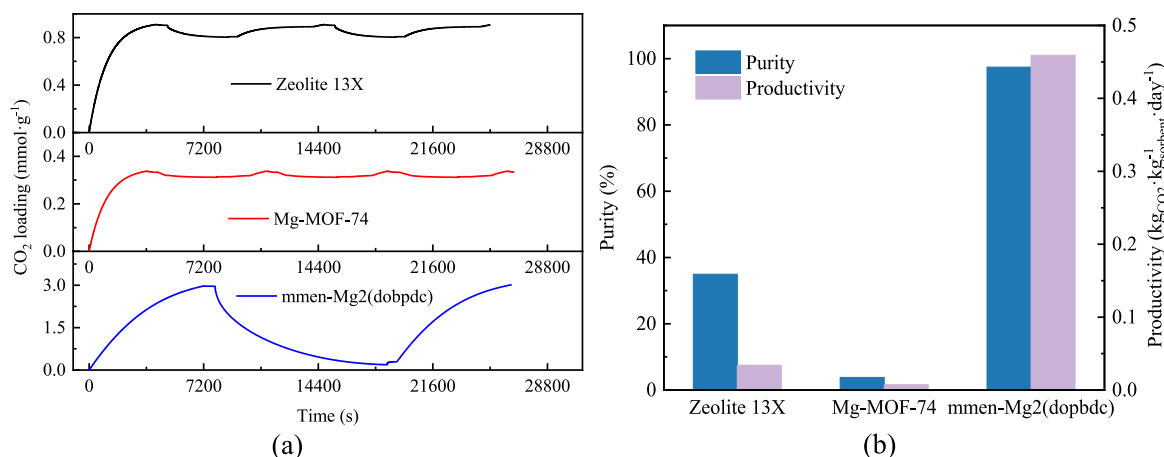
Fig. 10. (a) CO_2 loadings as a function of time at 373 K, (b) Purity and daily productivity of CO_2 product for three different sorbents.
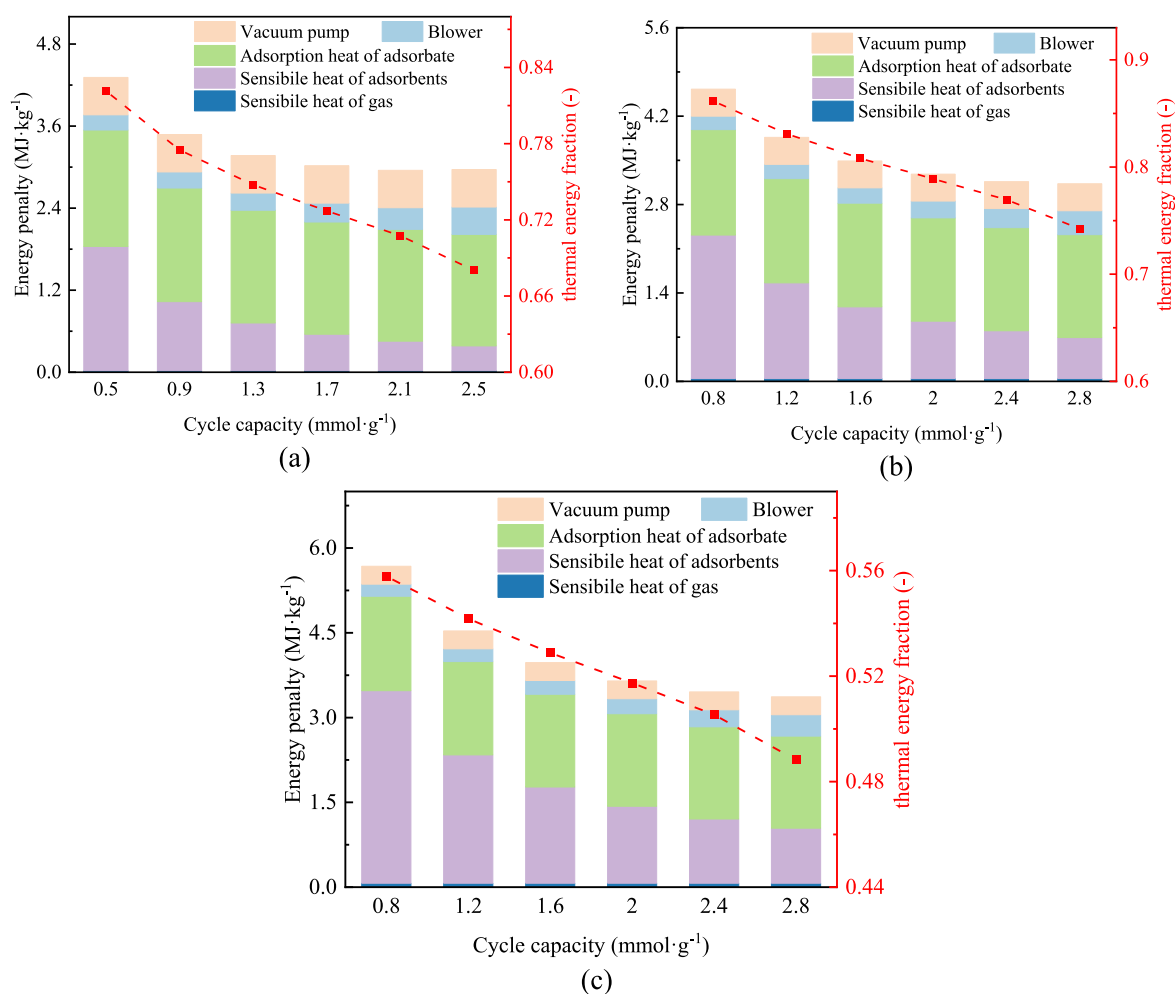
Fig. 11. Energy penalty and thermal energy fraction with change of working capacity at (a) 323 K, (b) 348 K, and (c) 373 K.

at 0.2 mmol g^{-1} for 348/373 K and 0.5 mmol g^{-1} at 323 K. The values can be further optimized. The inlet air velocity in the adsorption step is another key factor in the energy penalty. This value is chosen at 0.5 m s^{-1}, referring to Fig. 5c.

Energy distribution for the TVSA processes is shown in Fig. 11. Total energy penalty rises as the increase in desorption temperatures. Meanwhile, the electricity consumption of vacuum pumps is reduced slightly for higher evacuation pressure. But it has no apparent effect on the trend

of the total energy penalty. It is attributed to the huge sensible heat of sorbents and therefore causes inevitable heat loss. The growth of working capacity can reduce the cycle numbers per unit mass of product and avoid excessive thermal energy penalty in sensible heat of sorbents. Blowers consume more electricity at higher working capacity. Thus, a decreasing trend of thermal energy fraction can be found in all cases in every subplot of Fig. 11. The optimal values of working capacity also exist. In related adsorption applications, it is well known that 90% of

equilibrium loading is regarded as a suitable value for the adsorption loading limit (Aristov et al., 2008).

If the desorption of N_2 is neglected, the energy penalty caused by the adsorption heat of CO_2 is approximately 1.63 MJ kg^{-1}. It takes up 54.0%, 52.1%, and 48.4% for the conditions at 2.5 mmol g^{-1}/323 K, 2.8 mmol g^{-1}/348 K, and 2.5 mmol g^{-1}/348 K, respectively. The value does not change with working capacity but is still the main source of energy penalty. There is also a notable condition that the desorption temperature is not equal to the average temperature in the adsorption bed. Endothermic effect by adsorption heat of adsorbate and heating boundary in the outer surface of bed co-create a radial temperature gradient. These phenomena limit kinetics in the desorption step, especially at higher temperatures. Fast kinetics at high temperatures will cause inevitable temperature drops and impede desorption efficiency due to the endothermic effect. Including mmen-Mg_2(dobpdc), functionalized sorbents usually own a high affinity with ultra-diluted CO_2. It not only makes higher equilibrium loading but also leads to larger heat of adsorption. It implies a trade-off in further design of sorbents to enhance the whole effectiveness of DAC.

In general, thermal energy fraction at all regeneration temperatures ranges from 48.8% to 86.2%, regarding the calculated results illustrated in Fig. 11. This suggests a great potential to reduce energy penalty by utilizing low-grade heat or renewables. For the specific condition at 2.4 mmol g^{-1}/373 K, without heat pump, heat demand for regeneration exceeds 2.84 MJ kg^{-1}, accounting for 82.1% of the total energy penalty. However, by utilizing heat pump, 1.75 MJ kg^{-1} of heat supply can be avoided at the expense of electricity demand of 1.09 MJ kg^{-1}. This decreases thermal energy fraction to 50.5%. Thus, as mentioned in Section 2, heating solutions can potentially bridge energy supply gap. Providing heat in DAC can be relatively costly, particularly when additional equipment is required. The capture cost of DAC is also constrained to different extents by different heating solutions. Therefore, it is still necessary to optimize cycle parameters for each case toward the cost for a more reasonable comparison. In the following section, a sensitivity analysis of economic performance is conducted to obtain detailed optimization of operating parameters.

4.4. Economic analysis of the DAC processes

4.4.1. Guidelines for economic evaluation of DAC

The effective sorbent, mmen-Mg_2(dobpdc), provides superiority for practical DAC application. The specific configurations of DAC plants vary from the desorption temperatures of the TVSA process according to what auxiliary equipment is used to help drive the TVSA cycle. Four solutions for the regeneration of sorbents have been proposed in Section 2.

Different process parameters of the DAC system can affect each other in economic performance. The main equipment of DAC plants includes blowers, adsorption contactors, vacuum pumps, heat exchangers, storage and compression, and auxiliary heating units. The capital and operation costs are detailed in **Supplementary Information Note S2 and Note S3**. The cost of the DAC system, when deployed in buildings, is also estimated by the levelized cost of DAC (LCOD), as shown in Eq. (25).

$$LCOD = \frac{CAPC_{sys} \cdot crf + FOC_{sys}}{m_{p,year}} + VOC_{sys} \qquad (25)$$

where $CAPC_{sys}$ ($) is the capital cost, FOC_{sys} ($\cdot year^{-1}$) is the fixed operation cost, VOC_{sys} ($\cdot kg^{-1}$) is the variable operation cost, $m_{p,year}$ ($t_{CO_2} \cdot year^{-1}$) is CO_2 production of a DAC plant in a working year, and *crf* is defined as capital recovery factor. Detailed calculation is explained in **Supplementary Information Note S4.**

Differences in CO_2 loading during the TVSA process will cause a change in time cost and size of the relevant equipment. It has a notable impact on LCOD. The analysis selects two typical adsorption loadings to form stable TVSA cycles, as shown in Fig. 12. Adsorption time and
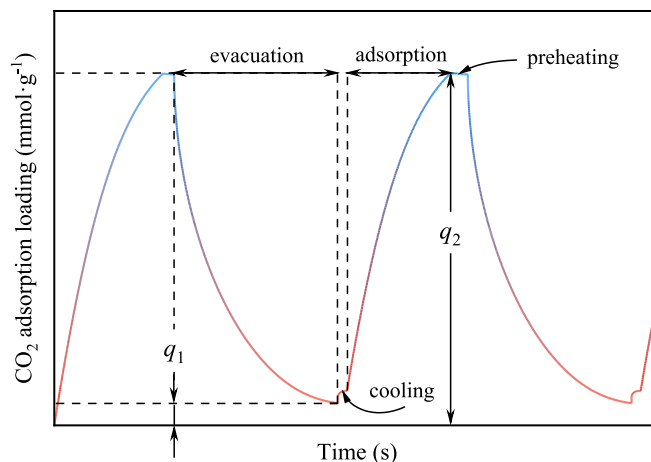
Fig. 12. Selection of adsorption loading and division of time for each process step.

desorption time are also determined with the help of the mathematical model previously established.

The guidelines provide a criterion for the analysis of economic performance. This section discusses multiple-dimensional influences on LCOD. The study tries to determine the optimal parameters of DAC during construction and operation from the view of economic performance. The optimized cases for different desorption temperatures are compared. LCOD is also predicted from 2022 to 2050 with the development of DAC.

4.4.2. Effects of module mass on LCOD

DAC is highly modular compared to conventional separation techniques in chemical engineering (McQueen et al., 2021). It means a DAC plant can be divided into multiple miniaturized units and helps for better organization and planning of working procedures. The capital cost of DAC plants varies from modular scale since the purchase cost of related auxiliary equipment does not show a linear relationship with the scale. The calculation assumes different module masses and explores the effect of module scale on LCOD. The parameters of calculated cases are listed in Table S6. As shown in Fig. 13, the expansion of single module mass can significantly reduce LCOD in all cases. It can be attributed that expanding module mass can improve the occupancy rate of the full
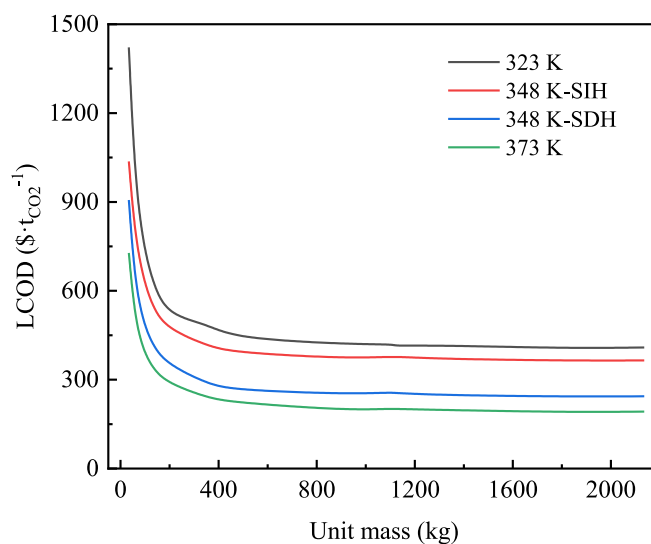
Fig. 13. LCOD variation as a function of module mass for cases at 323 K, 348 K–SIH, 348 K-SDH, and 373 K.

capacity of each equipment and thus achieve cost reduction. But from 931.2 kg to 2207 kg per module, LCODs at 323 K, 348 K for solar district heating, 348 K for solar individual heating, and 373 K vary from 420.6 $\cdot t_{CO_2}^{-1}$, 372.4 $\cdot t_{CO_2}^{-1}$, 251.7 $\cdot t_{CO_2}^{-1}$, and 197.3 $\cdot t_{CO_2}^{-1}$ to 408.7 $\cdot t_{CO_2}^{-1}$, 365 $\cdot t_{CO_2}^{-1}$, 244.2 $\cdot t_{CO_2}^{-1}$, and 192.4 $\cdot t_{CO_2}^{-1}$ respectively. Excessive expansion of a single unit means a higher workload of process equipment. It requires increasing device numbers and causes higher costs for each unit. Thus, the effect of scaling up on the cost reduction is limited though the volume of sorbents is still acceptable. The results suggest to uses a module mass of 931.2 kg, equivalent to a 1.5 m*1.5 m*1.5 m contactor. The adopted scale of a single module can capture 136.1 t_{CO_2}·year^{-1}. In the first commercial DAC plant built by Climeworks (Climeworks), 18 modules are designed to produce 900 t_{CO_2}·year^{-1}. The size of a single module can be roughly estimated at 1.47 m*1.47 m*1.47 m (Gebald et al., 2017; Sabatino et al., 2021). The proposed scale is feasible for industrial practice and achieves better productivity due to the high working capacity of mmen-Mg_2(bodpdc).

4.4.3. Effects of evacuation pressure on LCOD

For DAC plants using mmen-Mg_2(bodpdc), vacuum pumps are essential components of the processing system. The equilibrium loading of CO_2 on sorbents is reduced and promotes the release of CO_2 at desorption temperatures by using vacuum pumps. A higher vacuum leads to lower equilibrium and improves desorption kinetics and working capacity, but it does not mean that the high vacuum process is beneficial for reducing LCOD. Low evacuation pressure requires more investment in vacuum pumps, and the electricity penalty will also greatly increase under the corresponding evacuation pressure. Hence, cost reduction of DAC requires optimization of the evacuation pressure towards LCOD.

The duration of each step is obtained from simulations in Section 3. The investment correlation for vacuum pumps is shown in Eq. (S15). Parameters for each case are listed in Table S7. Results can be seen in Fig. 14. LCODs for different heating solutions show obvious discrepancies, which will be discussed in the following sections. For the case of desorption temperature at 373 K, LCOD is 232.5 $\cdot t_{CO_2}^{-1}$ at 4800 Pa and 201.1 $\cdot t_{CO_2}^{-1}$ at 4000 Pa. LCOD shows a positive relation with evacuation pressure, which is lower than step pressure in isotherm model. Productivity is enhanced due to faster kinetic, but negative cost factors on LCOD, such as larger vacuum pump capacity, have a minor influence. When evacuation pressure is lower than 3500 Pa, the effects are reversed. The case of 121 Pa shows the working capacity of vacuum
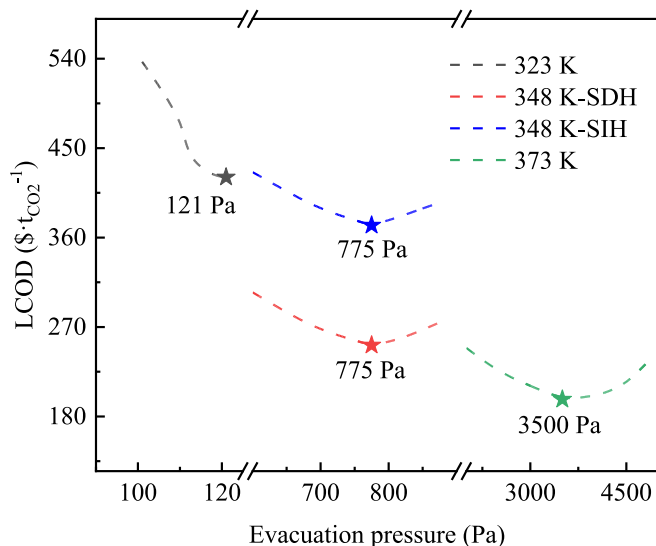
Fig. 14. LCOD variation as a function of evacuation pressure for cases at 323 K, 348 K–SIH, 348 K-SDH, and 373 K.

pumps has a more dominant effect. Fig. 14 indicates that optimal evacuation pressures are 121 Pa for 323 K, 775 Pa for 348 K-SDH and 348 K–SIH, and 3500 Pa for 373 K.

4.4.4. Effects of inlet air velocity on LCOD

In the proposed TVSA process, blowers propel air through the contactor. Because sorbents have poor mass transfer ability, demand for feed gas air is high at the adsorption step. Blower's working hours account for more than 50% of the total duration of the cycle. Fig. 11 in section 4.3 indicates that blowers consume 47.0% and 21.9% of the total electricity penalty. To investigate the effects of inlet air velocity on LCOD, it is selected from 0 to 2 m s^{-1}. Air velocities can determine the duration of the adsorption step by simulation method and be further input for economic analysis to calculate LCOD. The mass of the contactor in the calculations is 931.2 kg, and the range of CO_2 loading is 0.3–3 mmol g^{-1}.

Fig. 15 shows the results of LCOD under different air velocities. LCOD significantly drops when air velocity increases from 0 m s^{-1} to 0.3 m s^{-1}. It shows appropriate velocity is important for adsorption promotion. From 0.05 m s^{-1} to 0.25 m s^{-1}, LCOD and productivity vary from 644.5 $\cdot t_{CO_2}^{-1}$/81.7 t_{CO_2}·year^{-1} to 432.9 $\cdot t_{CO_2}^{-1}$/125.4 t_{CO_2}·year^{-1} at 323 K/121 Pa, and 451.5 $\cdot t_{CO_2}^{-1}$/9.8 t_{CO_2}·year^{-1} to 396.2 $\cdot t_{CO_2}^{-1}$/173.7 t_{CO_2}·year^{-1} at 348 K–SIH/750 Pa of desorption conditions. Other conditions follow a similar tendency. But extremely high velocities are invalid for the reduction of LCOD. It needs more feed gas due to the low heat utilization of air though the kinetic of adsorption can indeed be improved. Fig. 15d indicates that a velocity of more than 0.5 m s^{-1} is ineffective on the duration of adsorption. But operation costs will increase due to high-pressure drop and volume flux of air through the contactor caused by high velocities. Considering the effect of air velocities on both productivity and LCOD, the optimal velocity of inlet air is the screen as 0.5 m s^{-1}, and the corresponding duration of adsorption is 7300 s.

4.4.5. Effects of CO_2 loadings on productivity and LCOD

The duration of a cycle has a significant impact on the productivity and LCOD of the DAC plant. Adsorption and desorption steps generally occupy more than 85% of the total time. To better investigate the impact of adsorption and desorption time, q_1 and q_2 are used as variations, and calculations on LCOD and productivity are conducted. The definition of q_1 and q_2 has been illustrated in section 4.4.1.

The parameters differ in cases due to the diversity in adsorption and desorption kinetics during the TVSA cycles. Contours with two different parameters are shown in Fig. 16. Optimization of productivity requires maximizing working capacity and minimizing the cycle period. Since the kinetics constants of desorption are larger than those of adsorption, it is advisable to set q_2 to close to equilibrium loadings, while q_1 tends to show a large gap with equilibrium loadings, even less than 80% of total adsorption capacity. This trend is more notable with the increase in desorption temperatures. The results indicate that optimal values of q_1 and q_2 towards productivity are 2.701/1.2 mmol g^{-1} at 323 K, 2.501/0.8 mmol g^{-1} at 348 K, and 2.407/0.2 mmol g^{-1} at 373 K. Meanwhile, productivity is achieved at 503.4 kg·day^{-1}, 715.5 kg·day^{-1}, 905.5 kg·day^{-1}, respectively.

The optimal parameters for LCOD are inconsistent with those for productivity. It is known that LCOD is related to productivity, but high productivity may also induce an additional cost on equipment. The calculation results can be obtained: the lowest LCOD could be achieved at 379.8 $\cdot t_{CO_2}^{-1}$ when 2.1/0.6162 mmol g^{-1} for cases of 323 K, 231.1 $\cdot t_{CO_2}^{-1}$ when 2.403/0.301 mmol g^{-1} for cases of 348 K-SDH, 1, 358.6 $\cdot t_{CO_2}^{-1}$ when 2.702/0.201 mmol g^{-1} for cases of 348 K–SIH, and 176.7 $\cdot t_{CO_2}^{-1}$ when 2.407/0.11 mmol g^{-1} for cases of 373 K.

4.4.6. Cost and prospect of DAC using mmen-Mg_2(dobpdc)

Based on the economic analysis, the working conditions of DAC using mmen-Mg_2(dobpdc) can be derived. The optimization of DAC is based
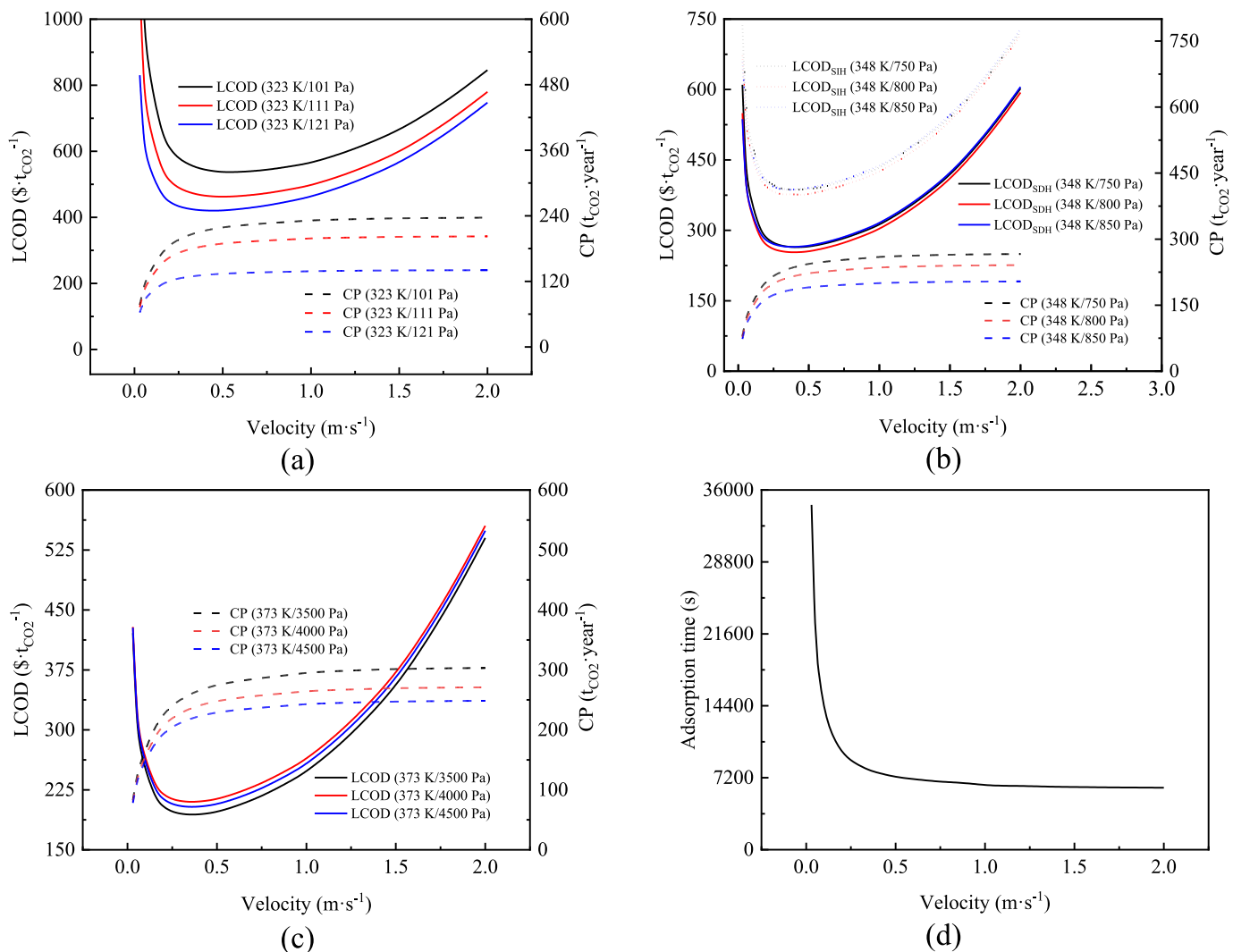
Fig. 15. LCOD variation as a function of inlet air velocity for cases at (a) 323 K, (b) 348 K–SIH and 348 K-SDH, and (c) 373 K. (d) duration of adsorption at 298 K as a function of inlet air velocity. CP: CO_2 production in a working year ($t_{CO2} \cdot year^{-1}$).

on LCOD with due consideration for productivity in a day. The obtained parameters for optimal working conditions in all cases are listed in Table 6. The mass of sorbents in the contactor is 931.2 kg.

LCOD is composed of capital and operation costs according to how investment is spent. Fig. 17 breaks down LCOD in different cases. The proportion of vacuum pump expenditure in capital cost is high. It can be attributed to the high-volume rate of the product, especially in the conditions for low evacuation pressure at low desorption temperatures. The cost of contactors includes expenditures of the reactor and sorbent manufacture. The sorbents may experience deterioration after repeated cycles, thus the lifespan of sorbents is set at 5 years at the cost of 50 $\cdot kg^{-1}$. However, this optimistic pricing choice still leads to high expenditure on sorbents. For example, under the condition of 373 K, the contactor with sorbents cost 55.8 $\cdot t_{CO2}^{-1}$, which account for 52.7% of the total capital cost. The high cost of sorbents can also be found in a summarization for the economic analysis in DAC (Wu, X. et al., 2022). Thus, it still demands cost retrenchment for mmen-Mg_2(dobpdc) and may also call for another economic-competitive sorbent with high working capacity and low cost. The capital and operation cost of auxiliary equipment for heating use is obtained from technology data compiled by Danish Energy Agency (Energistyrelsen, 2022), also provided in **Supplementary Information Note S2**. Although thermal energy demand at 373 K is high, from Fig. 17a, using heat pumps is still attractive in terms of capital cost, roughly equivalent to blowers.

The cost for 348 K-SDH is lower than that of 348 K–SIH. It can be attributed to the cost reduction brought by centralization and scale-up, especially in operation, as shown in Fig. 17b. But solar district heating has a high threshold of thermal capacity. And infrastructure construction needs to be carried out in advance. The total scale of DAC by solar district heating should be large enough, or deployed buildings have other demand for solar heating. These factors make DAC less flexible in scaling and location of deployment. But generally, solar district heating is more appropriate for DAC from the economic perspective. The case of 323 K utilizes condensation heat in the HVAC system. Although thermal energy is recycled at near-zero cost and operation cost is reduced, it is still not an economic-competitive solution for DAC in buildings due to investment in vacuum pumps. Productivity is also considered for DAC in buildings with the low-grade heat utilization. There is a trend that cases with higher desorption temperatures achieve the higher productivity, known from Table 6. It is caused by the kinetics at the higher desorption temperatures.

Comprehensively considering LCOD, productivity, and temperature of heat utilization, priority is suggested to be given to the cases using heat pumps for auxiliary heating. Using heat pumps is a universal solution for heating. Although it can only achieve high temperatures output at the expense of electricity, this approach decreases capital cost at low desorption temperatures. It can still utilize various low-grade heat in the buildings, such as cooling water of the HVAC system. Meanwhile,

(a)

(b)

(c)

(d)

(e)

(f)
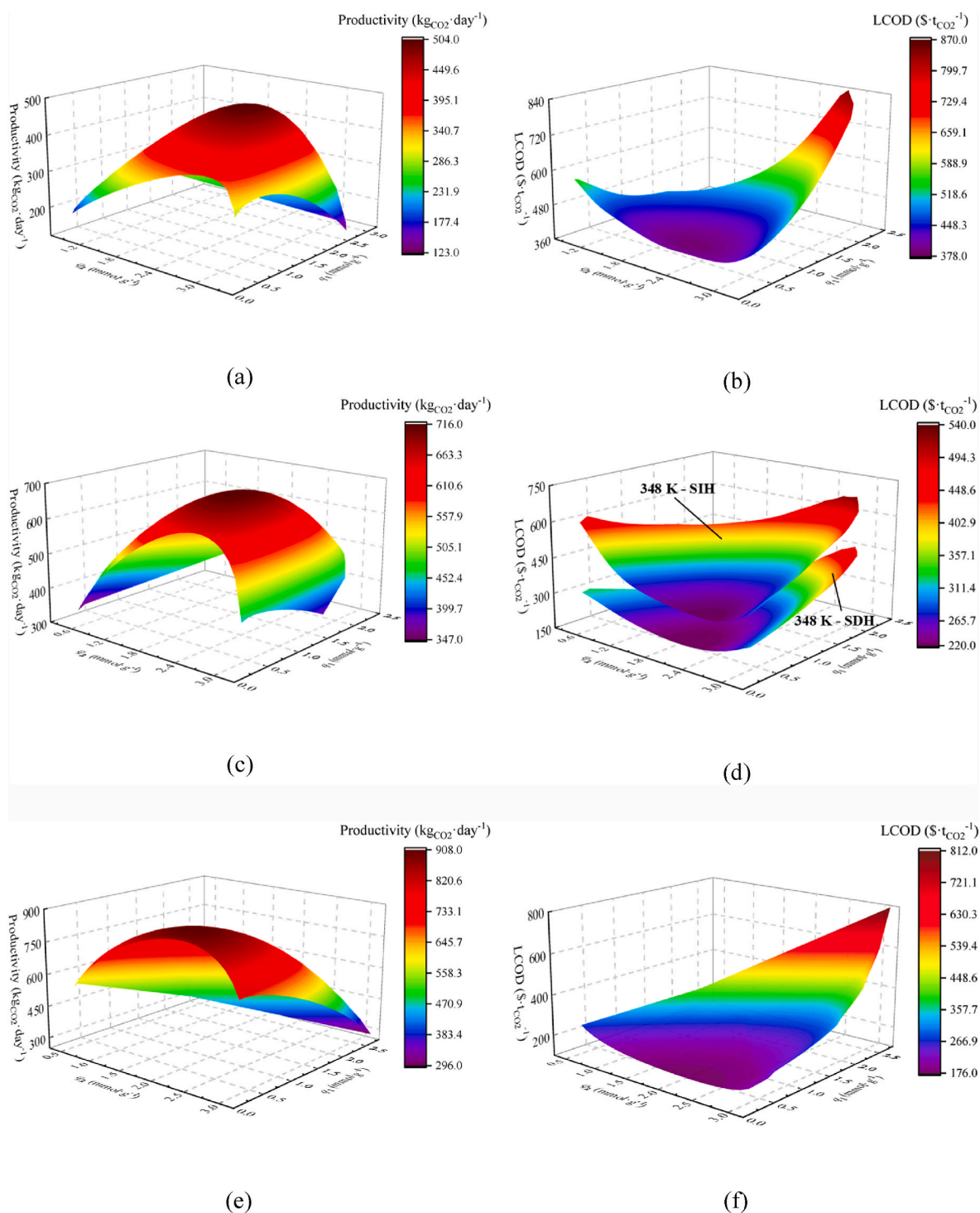
Fig. 16. Two parameters analysis with effect of q_1 and q_2 on productivity in a day at (a) 323 K, (c) 348 K, (e) 373 K, and on LCOD at (b) 323 K, (d) 348 K, and (f) 373 K.

this technology has been well integrated and mature and can be applied in either distribution or centralization. The scale can be adjusted flexibly as the deployment of DAC.

The economic analysis calculates the expenditures of the proposed DAC in detail. To demonstrate the advantages of DAC with low-grade heat utilization and further reflect the difference between four solutions, calculations considering CO_2 emissions when the operation is conducted. The base case assumes that heat for regeneration is provided by natural gas boiler. The carbon intensity is used to evaluate emission

and capture ratio, as listed in Table S13. The following analysis defines net LCOD, as interpreted in **Supplementary Information Note S5**.

Effects of CO_2 emissions and initial LCOD on the net levelized cost of DAC (net LCOD) for all four cases are investigated in Fig. 18. It is obvious that the base case has lower LCOD except the case of 323 K, because of cheaper investment and operation than low-grade heat or renewables. The comparison changes when emissions from energy supply are considered. The net LCOD is enhanced by 25.0%, 17.7%, and 5.2% in the case of 323 K, 348 – SDH and 373 K, respectively. The case of solar

Table 6
Optimal parameters for DAC in all cases.

Cases	v_{air}	t_{ad}	t_{ev}	t_{cool}/t_{ph}	LCOD	$m_{CO_2,day}$
323 K/121 Pa	0.5 m s^{-1}	3974 s	8152 s	720/ 600 s	398.7 $\cdot t_{CO2}^{-1}$	442.3 kg·day^{-1}
348 K–SIH/ 775 Pa	0.5 m s^{-1}	5545 s	5736 s	720/ 600 s	364.7 $\cdot t_{CO2}^{-1}$	656.7 kg·day^{-1}
348 K-SDH/ 775 Pa	0.5 m s^{-1}	4553 s	5006 s	720/ 600 s	237.1 $\cdot t_{CO2}^{-1}$	670.1 kg·day^{-1}
373 K/3500 Pa	0.5 m s^{-1}	4450 s	3001 s	720/ 600 s	176.7 $\cdot t_{CO2}^{-1}$	893.6 kg·day^{-1}

individual heating seems not suitable for DAC from the net LCOD perspective. Its low carbon intensity cannot make up for its high cost, causing less cost-effectiveness than the base case. When heat pumps are used to regenerate TVSA processes, they will inevitably consume electricity to drive heating, which makes improvement small. Moreover, the electricity consumption will exceed 20% in a complete cycle of the DAC process. It may require additional solutions for low-carbon electricity generation in buildings, such as solar photovoltaics. Moreover, utilizing low-grade heat also offers the advantage of improving energy security. Natural gas supply is vulnerable to geopolitics, which is an unstable factor for pricing and transport. The results show that DAC with low-grade heat utilization in buildings can reduce CO_2 emissions during DAC processes and achieve better negative emission effects for carbon capture. Although the LCODs gap between the different cases has been narrowed, regeneration at 373 K using heat pumps is numerically still the most competitive solution for DAC in buildings.

Fig. 19 shows the results of LCOD prediction in 2030, 2040, and 2050. The prediction method is introduced in **Supplementary Information Note S6** and is based on learning theory. LCOD is reduced as the scale increase over the years, and the cost of all four solutions tends to be similar. According to the current state of technology, the cost of DAC ranges from 250 $\cdot t^{-1}$ to 600 $\cdot t^{-1}$ (Ozkan et al., 2022b), depending on energy supply, locations, policy and so on. It indicates that regeneration by heat pumps is the most economical solution in the current stage. Other cases are numerically within a reasonable range. But by 2030 and 2040, regeneration by solar district heating can also be competitive. From Fig. 19, by 2050, the cases of regeneration by solar district heating and heat pumps can meet cost target of 100 $\cdot t_{CO2}^{-1}$ set by the industry, while the LCOD of 323 K and 338 K–SIH is 123 $\cdot t^{-1}$ and 133 $\cdot t^{-1}$. The gap is understandable because the related calculations of LCOD use a generic learning rate for DAC. For novel sorbents in this work, i.e., mmen-Mg$_2$(dobpdc), the learning rate can be estimated to exceed 30%. Besides, the profitable threshold for DAC is also highly related to energy policy. For example, the government provides tax rebates at 50 $\cdot t_{CO2}^{-1}$
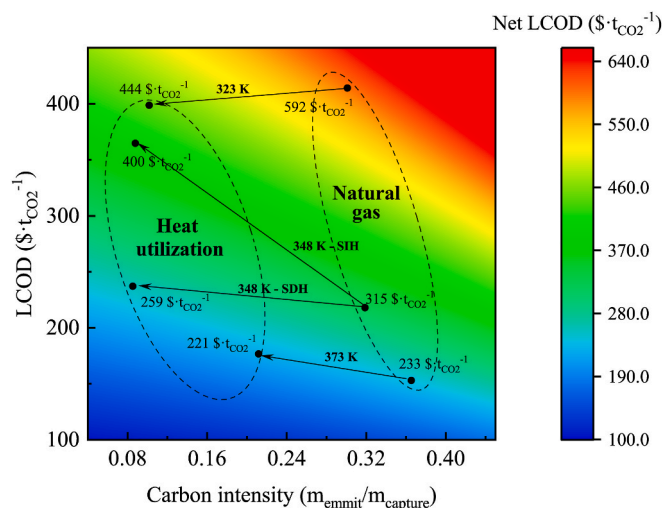
Fig. 18. Effects of CO_2 emissions and initial LCOD on net levelized cost of DAC.
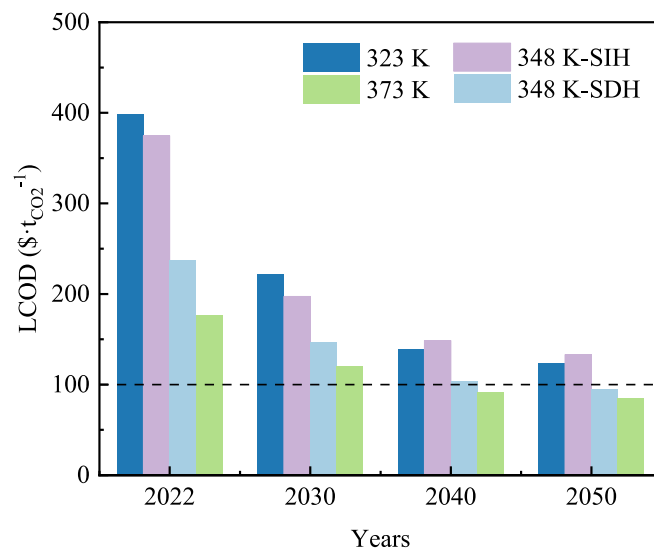
Fig. 19. Development of LCOD for all cases according to CO_2 emission prediction.
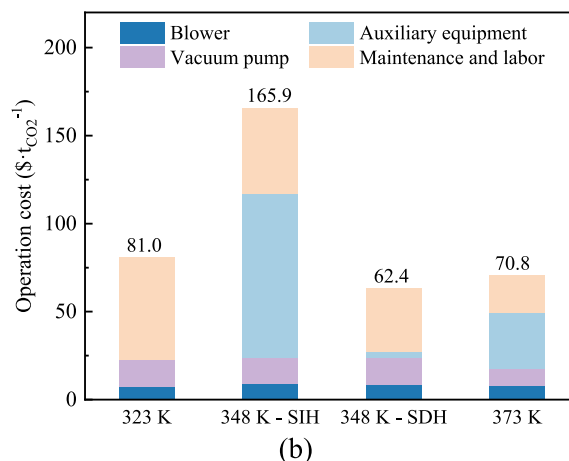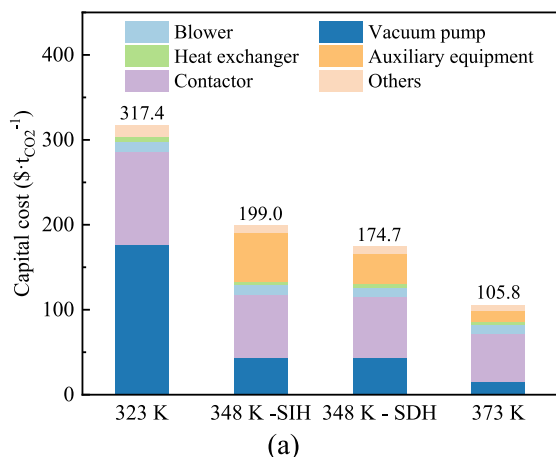
Fig. 17. LCOD breakdown into equipment for average (a) capital cost and (b) operation cost.

for CO_2 storage (a process after direct air capture) in the United States (Meckling and Biber, 2021). In regions with aggressive carbon pricing policies, such as Norway (229 $\$\cdot t_{CO_2}^{-1}$ by 2030), Ireland (111 $\$\cdot t_{CO_2}^{-1}$ by 2030), and Canada (136 $\$\cdot t_{CO_2}^{-1}$ by 2030), the gap can be possibly filled (WorldBank, 2022). It indicates that four cases, particularly heating by heat pumps and solar district heating, have the potential to meet the industrial target by 2050. With ration configurations of low-grade heat and renewables, the application of DAC and diversity of heat sources can be enhanced, which can provide incentives for DAC with low-grade heat utilization in buildings.

5. Conclusion

The goal of this study is to investigate a TVSA process for DAC with four heating solutions by using low-grade heat or renewables in buildings. Although the concept and system were proposed, the analysis of LCOD and the selection of solutions are rare. This study aims to bridge cycle performance and economic feasibility in the integrated DAC based on a detailed numerical model using mmen-Mg_2(dobpdc). The conclusions are as follows:

(1) The durations of TVSA process are estimated. Adsorption step takes 7200 s with 0.6 m s^{-1} of inlet air velocity. After preheating for 720 s, the packed bed is evacuated to extract CO_2 for 10800 s, and ends up with a cooling for 600 s. Total duration is primarily estimated at around 5 h 22 min. The chosen sorbents, mmen-Mg_2(dobpdc), show a good performance regarding purity and productivity compared with Zeolite 13X and Mg-MOF-74, which shows the advantages of the high capacity.

(2) Energy penalty in the proposed heating solutions for 323 K, 348 K, and 373 K are analyzed. The thermal energy fraction in the TVSA process ranges from 48.8% to 86.2%. The vacuum pump decreases its electricity consumption from 0.55 MJ kg^{-1}/323 K to 0.32 MJ kg^{-1}/373 K, indicating that lower temperatures increased the workload. The energy distribution shows that heat consumed by sorbents is always a dominant factor for all temperatures, leaving a huge space to reduce the thermal consumption.

(3) LCODs in four heating solutions for DAC are optimized. LCOD with low-grade heat is 398.7 $\$\cdot t_{CO_2}^{-1}$ for regeneration by condensation heat in HVAC, 364.7 $\$\cdot t_{CO_2}^{-1}$ for solar individual heating, 237.1 $\$\cdot t_{CO_2}^{-1}$ for solar district heating, and 176.7 $\$\cdot t_{CO_2}^{-1}$ for heat pumps, respectively. The LCODs are broken down into each equipment and show that vacuum pumps incur a proliferating cost at lower temperatures due to low pressure demand and undesirable kinetics. Regeneration by solar individual heating indicates a high cost in the operation of heating equipment. Thus, from an economic perspective, using heat pumps is the best solution for low-grade heat utilization.

(4) The net LCODs, which consider carbon emission in the process, are determined. The low-grade heat utilization in buildings will reduce the net carbon emission in DAC compared with natural gas driven systems. The net LCOD is enhanced by 25.0%, 17.7%, and 5.2% in the case of 323 K, 348 – SDH, and 373 K, respectively. Using heat pumps to regenerate sorbents consumes more electricity but is still the most competitive solution from the net LCOD. Based on learning rates, LCOD for using solar district heating and heat pumps can be decreased to the target of 100 $\$\cdot t_{CO_2}^{-1}$ set by the industry. This economically proves the high potential of low-grade heat to integrate with DAC in buildings.

The results provide suggestive guidelines for the viability of DAC in buildings from a techno-economic aspect. The techno-economic model in this work is partly simplified. For example, we do not include the water co-adsorption effect, because the existing dehumidification devices in HVAC can dry the inlet air. In future research, integrated porotypes should be developed, and trial runs are suggested for validation. Other factors (such as dynamic concentrations, hybrid energy configurations) can also be explored to advance the application further.

CRediT authorship contribution statement

W.K. Shi: Conceptualization, Data curation, Formal analysis, Investigation, Methodology, Roles/Writing-original draft, Writing – review & editing. **X.J. Zhang:** Investigation, Methodology, Project administration, Supervision. **X.Y. Liu:** Funding acquisition. **S. Wei:** Funding acquisition, Writing – review & editing. **X. Shi:** Funding acquisition, Software, Writing – review & editing. **C. Wu:** Funding acquisition, Project administration, Software. **L. Jiang:** Conceptualization, Data curation, Formal analysis, Funding acquisition, Investigation, Methodology, Project administration, Software, Supervision, Roles/Writing-original draft, Writing – review & editing.

Declaration of competing interest

The authors declare that they have no known competing financial interests or personal relationships that could have appeared to influence the work reported in this paper.

Data availability

Data will be made available on request.

Acknowledge

Appendix A. Supplementary data

Supplementary data to this article can be found online at https://doi.org/10.1016/j.jclepro.2023.137731.

References

Al-Janabi, N., Hill, P., Torrente-Murciano, L., Garforth, A., Gorgojo, P., Siperstein, F., Fan, X., 2015. Mapping the Cu-BTC metal–organic framework (HKUST-1) stability envelope in the presence of water vapour for CO2 adsorption from flue gases. Chem. Eng. J. 281, 669–677.

Aristov, Y.I., Dawoud, B., Glaznev, I., Elyas, A., 2008. A new methodology of studying the dynamics of water sorption/desorption under real operating conditions of adsorption heat pumps: experiment. Int. J. Heat Mass Tran. 51 (19–20), 4966–4972.

Baboolal, J.D., 2015. Evaluation of Novel Metal-Organic Framework Materials for Adsorptive Post-combustion CO2 Capture.

Bajamundi, E., J, C., Koponen, J., Ruuskanen, V., Elfving, J., Kosonen, A., Kauppinen, J., Ahola, J., 2019. Capturing CO2 from air: technical performance and process control improvement. J. CO2 Util. 30, 232–239.

Ben-Mansour, R., Qasem, N.A., 2018. An efficient temperature swing adsorption (TSA) process for separating CO2 from CO2/N2 mixture using Mg-MOF-74. Energy Convers. Manag. 156, 10–24.

Ben-Mansour, R., Habib, M., Bamidele, O., Basha, M., Qasem, N., Peedikakkal, A., Laoui, T., Ali, M., 2016. Carbon capture by physical adsorption: materials, experimental investigations and numerical modeling and simulations–a review. Appl. Energy 161, 225–255.

Ben-Mansour, R., Basha, M., Qasem, N.A., 2017. Multicomponent and multi-dimensional modeling and simulation of adsorption-based carbon dioxide separation. Comput. Chem. Eng. 99, 255–270.

Board, O.S., National Academies of Sciences, E., Medicine, 2019. Negative Emissions Technologies and Reliable Sequestration: A Research Agenda.

Breyer, C., Fasihi, M., Aghahosseini, A., 2020. Carbon dioxide direct air capture for effective climate change mitigation based on renewable electricity: a new type of energy system sector coupling. Mitig. Adapt. Strategies Glob. Change 25 (1), 43–65.

Brilman, W., Alba, L.G., Veneman, R., 2013. Capturing atmospheric CO2 using supported amine sorbents for microalgae cultivation. Biomass Bioenergy 53, 39–47.

Busch, 2022. Busch R5 KB 0020–0040 D/F|Busch United States. https://www.busch vacuum.com/us/en/products/r5-kb-0020-0040-d-f.html?product_technical_data =US_60.

Climeworks. Climeworks builds first commercial-scale direct air capture plant. https ://climeworks.com/news/climeworks-builds-first-commercial-scale-direct-air-capt ure-plant.

Copco, A.. Dry screw vacuum pump - Atlas Copco India. https://www.atlascopco.co m/en-in/vacuum-solutions/products/dry-vacuum-pumps/dry-screw-vacuum-pumps /DHS-065-200-VSD. (Accessed 18 August 2022).

Cousin-Saint-Remi, J., Denayer, J.F., 2017. Applying the wave theory to fixed-bed dynamics of Metal-Organic Frameworks exhibiting stepped adsorption isotherms: water/ethanol separation on ZIF-8. Chem. Eng. J. 324, 313–323.

Dantas, T.L., Luna, F.M.T., Silva Jr., I.J., Torres, A.E.B., de Azevedo, D.C., Rodrigues, A. E., Moreira, R.F., 2011. Carbon dioxide–nitrogen separation through pressure swing adsorption. Chem. Eng. J. 172 (2–3), 698–704.

Darunte, L.A., 2018. Application of Metal Organic Frameworks (MOFs) to Capturing CO2 Directly from Air. Georgia Institute of Technology.

Darunte, L.A., Terada, Y., Murdock, C.R., Walton, K.S., Sholl, D.S., Jones, C.W., 2017. Monolith-supported amine-functionalized Mg2 (dobpdc) adsorbents for CO2 capture. ACS Appl. Mater. Interfaces 9 (20), 17042–17050.

Darunte, L.A., Sen, T., Bhawanani, C., Walton, K.S., Sholl, D.S., Realff, M.J., Jones, C.W., 2018. Moving beyond adsorption capacity in design of adsorbents for CO2 capture from ultradilute feeds: kinetics of CO2 adsorption in materials with stepped isotherms. Ind. Eng. Chem. Res. 58 (1), 366–377.

Elfving, J., Bajamundi, C., Kauppinen, J., Sainio, T., 2017. Modelling of equilibrium working capacity of PSA, TSA and TVSA processes for CO2 adsorption under direct air capture conditions. J. CO2 Util. 22, 270–277.

Energistyrelsen, 2022. Technology data. https://ens.dk/en/our-services/projections-and -models/technology-data. (Accessed 10 January 2022).

Erans, M., Sanz-Pérez, E.S., Hanak, D.P., Clulow, Z., Reiner, D.M., Mutch, G.A., 2022. Direct air capture: process technology, techno-economic and socio-political challenges. Energy Environ. Sci. 15 (4), 1360–1405.

Fahr, S., Powell, J., Favero, A., Giarrusso, A.J., Lively, R.P., Realff, M.J., 2022. Assessing the physical potential capacity of direct air capture with integrated supply of low-carbon energy sources. Greenhouse Gases: Sci. Technol. 12 (1), 170–188.

Farooq, S., Ruthven, D.M., 1990. Heat effects in adsorption column dynamics. 2. Experimental validation of the one-dimensional model. Ind. Eng. Chem. Res. 29 (6), 1084–1090.

Fasihi, M., Efimova, O., Breyer, C., 2019. Techno-economic assessment of CO2 direct air capture plants. J. Clean. Prod. 224, 957–980.

Fuller, E.N., Schettler, P.D., Giddings, J.C., 1966. New method for prediction of binary gas-phase diffusion coefficients. Ind. Eng. Chem. 58 (5), 18–27.

Gebald, C., Piatkowski, N., Rüesch, T., Wurzbacher, J.A., 2017. Low-pressure drop structure of particle adsorbent bed for adsorption gas separation process. Google Patents.

Hefti, M., Joss, L., Bjelobrk, Z., Mazzotti, M., 2016. On the potential of phase-change adsorbents for CO 2 capture by temperature swing adsorption. Faraday Discuss 192, 153–179.

Hong, W.Y., 2022. A Techno-Economic Review on Carbon Capture, Utilisation and Storage Systems for Achieving a Net-Zero CO2 Emissions Future. Carbon Capture Science & Technology, 100044.

Hughes, R., Kotamreddy, G., Ostace, A., Bhattacharyya, D., Siegelman, R.L., Parker, S.T., Didas, S.A., Long, J.R., Omell, B., Matuszewski, M., 2021. Isotherm, kinetic, process modeling, and techno-economic analysis of a diamine-appended metal–organic framework for CO2 Capture using fixed bed contactors. Energy Fuels 35 (7), 6040–6055.

IEA, 2022. The Future of Heat Pumps. IEA, Paris.

Ji, Y., Yong, J., Liu, W., Zhang, X., Jiang, L., 2023. Thermodynamic analysis on direct air capture for building air condition system: balance between adsorbent and refrigerant. Energy and Built Environment 4 (4), 399–407.

Jiang, L., Gonzalez-Diaz, A., Ling-Chin, J., Roskilly, A., Smallbone, A., 2019. Post-combustion CO2 capture from a natural gas combined cycle power plant using activated carbon adsorption. Appl. Energy 245, 1–15.

Jiang, J., Hu, B., Wang, R., Deng, N., Cao, F., Wang, C.-C., 2022. A review and perspective on industry high-temperature heat pumps. Renew. Sustain. Energy Rev. 161, 112106.

Jiang, L., Liu, W., Wang, R., Gonzalez-Diaz, A., Rojas-Michaga, M., Michailos, S., Pourkashanian, M., Zhang, X., Font-Palma, C., 2023. Sorption direct air capture with CO2 utilization. Prog. Energy Combust. Sci. 95, 101069.

Kasotia, P., 2007. The Health Effects of Global Warming: Developing Countries Are the Most Vulnerable. UN Chronicle.

Kim, M.K., Baldini, L., Leibundgut, H., Wurzbacher, J.A., Piatkowski, N., 2015. A novel ventilation strategy with CO2 capture device and energy saving in buildings. Energy Build. 87, 134–141.

Kim, M.K., Baldini, L., Leibundgut, H., Wurzbacher, J.A., 2020. Evaluation of the humidity performance of a carbon dioxide (CO2) capture device as a novel ventilation strategy in buildings. Appl. Energy 259, 112869.

Kumar, A., Madden, D.G., Lusi, M., Chen, K.J., Daniels, E.A., Curtin, T., Perry IV, J.J., Zaworotko, M.J., 2015. Direct air capture of CO2 by physisorbent materials. Angew. Chem. Int. Ed. 54 (48), 14372–14377.

Kumar, A., Hua, C., Madden, D.G., O'Nolan, D., Chen, K.-J., Keane, L.-A.J., Perry, J.J., Zaworotko, M.J., 2017. Hybrid ultramicroporous materials (HUMs) with enhanced stability and trace carbon capture performance. Chem. Commun. 53 (44), 5946–5949.

Lackner, K.S., 2013. The thermodynamics of direct air capture of carbon dioxide. Energy 50, 38–46.

Leonzio, G., Fennell, P.S., Shah, N., 2022. A comparative study of different sorbents in the context of direct air capture (DAC): evaluation of key performance indicators and comparisons. Appl. Sci. 12 (5), 2618.

Li, C., Shi, H., Cao, Y., Kuang, Y., Zhang, Y., Gao, D., Sun, L., 2015. Modeling and optimal operation of carbon capture from the air driven by intermittent and volatile wind power. Energy 87, 201–211.

Li, S., Deng, S., Zhao, L., Zhao, R., Lin, M., Du, Y., Lian, Y., 2018. Mathematical modeling and numerical investigation of carbon capture by adsorption: literature review and case study. Appl. Energy 221, 437–449.

Lian, Y., Deng, S., Li, S., Guo, Z., Zhao, L., Yuan, X., 2019. Numerical analysis on CO2 capture process of temperature swing adsorption (TSA): optimization of reactor geometry. Int. J. Greenh. Gas Control 85, 187–198.

Liu, D., Purewal, J., Yang, J., Sudik, A., Maurer, S., Mueller, U., Ni, J., Siegel, D., 2012. MOF-5 composites exhibiting improved thermal conductivity. Int. J. Hydrogen Energy 37 (7), 6109–6117.

Mason, J.A., McDonald, T.M., Bae, T.-H., Bachman, J.E., Sumida, K., Dutton, J.J., Kaye, S.S., Long, J.R., 2015. Application of a high-throughput analyzer in evaluating solid adsorbents for post-combustion carbon capture via multicomponent adsorption of CO2, N2, and H2O. J. Am. Chem. Soc. 137 (14), 4787–4803.

McDonald, T.M., Lee, W.R., Mason, J.A., Wiers, B.M., Hong, C.S., Long, J.R., 2012. Capture of carbon dioxide from air and flue gas in the alkylamine-appended metal–organic framework mmen-Mg2 (dobpdc). J. Am. Chem. Soc. 134 (16), 7056–7065.

McDonald, T.M., Mason, J.A., Kong, X., Bloch, E.D., Gygi, D., Dani, A., Crocella, V., Giordanino, F., Odoh, S.O., Drisdell, W.S., 2015. Cooperative insertion of CO2 in diamine-appended metal-organic frameworks. Nature 519 (7543), 303–308.

McQueen, N., Gomes, K.V., McCormick, C., Blumanthal, K., Pisciotta, M., Wilcox, J., 2021. A review of direct air capture (DAC): scaling up commercial technologies and innovating for the future. Progress in Energy 3 (3), 032001.

Meckling, J., Biber, E., 2021. A policy roadmap for negative emissions using direct air capture. Nat. Commun. 12 (1), 1–6.

Miao, Y., He, Z., Zhu, X., Izikowitz, D., Li, J., 2021. Operating temperatures affect direct air capture of CO2 in polyamine-loaded mesoporous silica. Chem. Eng. J. 426, 131875.

Mukherjee, S., Sikdar, N., O'Nolan, D., Franz, D.M., Gascón, V., Kumar, A., Kumar, N., Scott, H.S., Madden, D.G., Kruger, P.E., 2019. Trace CO2 capture by an ultramicroporous physisorbent with low water affinity. Sci. Adv. 5 (11), eaax9171.

Ozkan, M., Akhavi, A.-A., Coley, W.C., Shang, R., Ma, Y., 2022a. Progress in carbon dioxide capture materials for deep decarbonization. Chem 8 (1), 141–173.

Ozkan, M., Nayak, S.P., Ruiz, A.D., Jiang, W., 2022b. Current Status and Pillars of Direct Air Capture Technologies. Iscience, 103990.

Pai, K.N., Baboolal, J.D., Sharp, D.A., Rajendran, A., 2019. Evaluation of diamine-appended metal-organic frameworks for post-combustion CO2 capture by vacuum swing adsorption. Separ. Purif. Technol. 211, 540–550.

Patton, A., Crittenden, B., Perera, S., 2004. Use of the linear driving force approximation to guide the design of monolithic adsorbents. Chem. Eng. Res. Des. 82 (8), 999–1009.

Persily, A., 2015. Challenges in developing ventilation and indoor air quality standards: the story of ASHRAE Standard 62. Build. Environ. 91, 61–69.

Qasem, N.A., Ben-Mansour, R., Habib, M.A., 2018. An efficient CO2 adsorptive storage using MOF-5 and MOF-177. Appl. Energy 210, 317–326.

Rezaei, F., Webley, P., 2009. Optimum structured adsorbents for gas separation processes. Chem. Eng. Sci. 64 (24), 5182–5191.

Ruthven, D.M., 1984. Principles of Adsorption and Adsorption Processes. John Wiley & Sons.

Ruthven, D.M., Xu, Z., 1993. Diffusion of oxygen and nitrogen in 5A zeolite crystals and commercial 5A pellets. Chem. Eng. Sci. 48 (18), 3307–3312.

Sabatino, F., Grimm, A., Gallucci, F., van Sint Annaland, M., Kramer, G.J., Gazzani, M., 2021. A comparative energy and costs assessment and optimization for direct air capture technologies. Joule 5 (8), 2047–2076.

Schellevis, H., van Schagen, T., Brilman, D., 2021. Process optimization of a fixed bed reactor system for direct air capture. Int. J. Greenh. Gas Control 110, 103431.

Shen, Y., Yang, H., 2022. Achieving reduced emission and enhanced air quality by designing a solar-driven indoor CO2 capture system. J. Clean. Prod. 379, 134869.

Shen, Y., Yang, H., 2023. Global performance analysis of a solar-driven indoor CO2/H2O capture system for air quality enhancement and cooling energy saving. Energy Convers. Manag. 280, 116831.

Soletair, 2022. Technical Specifications of Building HVAC Integrated Direct Air Capture Unit – How Ventilation CO2 Capture Works. https://www.soletairpower.fi/technica l-specs-of-hvac-unit-soletair-power/. (Accessed 13 April 2023).

Wang, W., Yang, T., Pan, Q., Dai, Y., Wang, R., Ge, T., 2022. All-day freshwater production enabled by an active continuous sorption-based atmospheric water harvesting system. Energy Convers. Manag. 264, 115745.

Wilson, S.M., 2022. High purity CO2 from direct air capture using a single TVSA cycle with Na-X zeolites. Separ. Purif. Technol. 294, 121186.

Wilson, S.M., Tezel, F.H., 2020. Direct dry air capture of CO2 using VTSA with faujasite zeolites. Ind. Eng. Chem. Res. 59 (18), 8783–8794.

WorldBank, 2022. State and Trends of Carbon Pricing 2022 (Washington, DC).

Wu, J., Zhu, X., Chen, Y., Wang, R., Ge, T., The Analysis and Evaluation of Direct Air Capture Adsorbents on the Material Characterization Level. Available at SSRN 4106086.

Wu, J., Zhu, X., Chen, Y., Wang, R., Ge, T., 2022. The analysis and evaluation of direct air capture adsorbents on the material characterization level. Chem. Eng. J. 450, 137958.

Wu, X., Krishnamoorti, R., Bollini, P., 2022. Technological options for direct air capture: a comparative process engineering review. Annu. Rev. Chem. Biomol. Eng. 13, 279–300.

Wurzbacher, J.A., Gebald, C., Brunner, S., Steinfeld, A., 2016. Heat and mass transfer of temperature–vacuum swing desorption for CO2 capture from air. Chem. Eng. J. 283, 1329–1338.

Yu, Q., Brilman, W., 2020. A radial flow contactor for ambient air CO2 capture. Appl. Sci. 10 (3), 1080.

Zeman, F., 2007. Energy and material balance of CO2 capture from ambient air. Environ. Sci. Technol. 41 (21), 7558–7563.

Zhang, Z., Ding, Q., Cui, J., Cui, X., Xing, H., 2021. High and selective capture of low-concentration CO2 with an anion-functionalized ultramicroporous metal-organic framework. Science China Materials 64 (3), 691–697.

Zhao, R., Liu, L., Zhao, L., Deng, S., Li, S., Zhang, Y., Li, H., 2019. Thermodynamic exploration of temperature vacuum swing adsorption for direct air capture of carbon dioxide in buildings. Energy Convers. Manag. 183, 418–426.

Zhu, X., Ge, T., Yang, F., Wang, R., 2021. Design of steam-assisted temperature vacuum-swing adsorption processes for efficient CO2 capture from ambient air. Renew. Sustain. Energy Rev. 137, 110651.